Erasmus Mundus Joint Master's Degree in

Surface, Electro, Radiation, & Photo Chemistry (EMJMD SERP+)

Synthesis and Characterization of Thiomolybdate Cluster-Based Complexes for Electrocatalytic Hydrogen Evolution Reaction

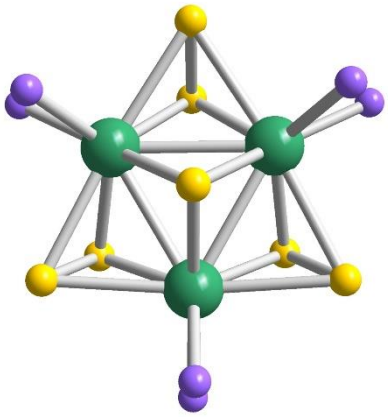

Christian Cariño

Supervisor: Prof. Emmanuel Cadot

Co-supervisors: Dr. Clément Falaise & Dr. Nathalie Guillou

February-July 2022

This page is intentionally left blank

Acknowledgements

My Master internship at Institut Lavoisier de Versailles was without a doubt an enriching experience. Apart from the laboratory work, I was given opportunities to present the results of my project in various occasions such as seminars and regular meetings with the ANR THIOMOF project team. I also had the chance to attend a three-day symposium in La Rochelle, France on the basics of polyoxometalate chemistry where I was able to interact with experts and young researchers in the field. Indeed, throughout my internship, not only did I hone my technical capabilities, but I also developed my skills in communication, and collaboration.

The completion of my thesis could not have been possible without the expertise of my supervisor, Prof. Emmanuel Cadot, to whom I am profoundly grateful. He allowed me to work independently while constantly offering insights and guidance. His boundless curiosity is inspiring, and it has been a privilege to be under his tutelage.

I would like to thank my co-supervisors, Dr. Clement Falaise and Dr. Nathalie Guillou, for their valuable insights and advice with the experiments and the interpretation of results. I also would like to express my gratitude to the following people who gave assistance and have important contributions to my work: Dr. Nathalie Leclerc for the TGA-FTIR and SEM-EDS, Dr. Jérôme Marrot for the single crystal XRD, Dr. Sergiu Calancea and Dr. Serge Albacha for the electrochemical experiments, Dmitri Konovalov for the hydrothermal MOF syntheses, and Maxence Lion for the gas chromatography.

I also greatly thank the European Commission and the Erasmus Mundus SERP+ program for generously funding my studies and for giving me this extraordinary privilege.

I am also extending my appreciation to my mentor in the University of the Philippines, Prof. Marlon Conato, who has provided me support at different stages of my career and for agreeing to be my referee.

My warm gratitude also goes to my colleagues and dearest friends, especially *Buonasera,* for filling my stay in Europe with wonderful memories. And finally, I am expressing my deepest gratitude to my best friend, Aaron, and my mother, Ma. Crispina, for being my constant source of inspiration, strength, and support.

List of Abbreviations

ANR	Agence Nationale de la Recherche	**{Mo_3}-ox**	$[Mo_3S_7(ox)_3]^{2-}$
CV	cyclic voltammetry	**NBu_4^+**	tetrabutylammonium cation
ΔG_{H^*}	Gibbs free energy of hydrogen binding	**NMR**	nuclear magnetic resonance
DMF	*N*,*N*,-dimethylformamide	**OER**	oxygen evolution reaction
dmit	1,3-dithia-2-thione-4,5-dithiolate	**ox**	oxalate
ECSA	electrochemically active surface area	**PEM**	proton exchange membrane
ESI-MS	electrospray ionization-mass spectrometry	**PXRD**	powder X-ray diffraction
FT-IR	Fourier-transform infrared	**TGA**	thermogravimetric analysis
GC	glassy carbon	**TOF**	turnover frequency
HDS	hydrodesulfurization	**TON**	turnover number
HER	hydrogen evolution reaction	**RHE**	reversible hydrogen electrode
HOPG	highly oriented pyrolytic graphite	**rpm**	revolutions per minute
HPLC-MS	high pressure liquid chromatography-mass spectrometry	**S_8**	elemental sulfur
LSV	linear sweep voltammetry	**SBU**	secondary building units
MicroGC	micro-gas chromatography	**UV-Vis**	ultraviolet-visible
MOF	metal-organic framework	**XPS**	X-ray photoelectron spectroscopy
MoSx	molybdenum sulfides	**XRD**	X-ray diffraction
{Mo_3}-dmit	$[Mo_3S_7(dmit)_3]^{2-}$		

Abstract (*English Version*)

Molybdenum sulfide materials (MoS_x) have been identified as cheap and efficient non-noble metal catalysts for hydrogen evolution reaction (HER). Molecular analogues of MoS_x based on thiomolybdate clusters have emerged as platforms for HER catalysis that can be utilized as active phases in electrode devices. In this work, we demonstrated the HER activity of two $\{Mo_3S_7\}$ cluster-based complexes ($[Mo_3S_7(dmit)_3]^{2-}$ (dmit = 1,3-dithia-2-thione-4,5-dithiolate) and $[Mo_3S_7(ox)_3]^{2-}$ (ox = oxalate)) by heterogeneous electrocatalytic reduction of protons. The complexes were prepared by straightforward wet chemical approaches and were characterized by single and powder X-ray diffraction (XRD) as well as thermogravimetric analysis (TGA). Glassy carbon electrode was modified with catalytic inks of the complexes by drop-casting technique and showed HER activity that depends on the composition of the ink (i.e., catalyst/carbon ratio, solvent, presence of Nafion®). The activity of $[Mo_3S_7(dmit)_3]^{2-}$ was found to increase with successive potential cycling and was demonstrated to remain stable for a period of 17 h. Meanwhile, although $[Mo_3S_7(ox)_3]^{2-}$ displays excellent HER activity initially, the catalyst undergoes electrochemical reduction and can desorb from the electrode surface leading to loss of activity with potential cycling. The study exemplifies the potential of thiomolybdate cluster complexes as HER electrocatalysts and highlights the modulating effect of the ligand on the activity and stability.

Abstract (*Version Française*)

Les matériaux à base de sulfures de molybdène (MoS_x) constitués d'éléments non noble, c'est-à-dire abondants et peu couteux sont des catalyseurs efficaces pour la réduction des protons en dihydrogène (HER). L'utilisation de clusters thiomolybdiques, véritables analogues moléculaires de ces sulfures de molybdène apparait comme un moyen efficace de manipuler, de fonctionnaliser et s'immobiliser ces phases actives dans des dispositifs d'électrode. Dans ce travail, nous avons étudié deux complexes de coordination construits sur le cluster $\{Mo_3S_7\}$ ($[Mo_3S_7(dmit)_3]^{2-}$ (dmit = 1,3-dithia-2-thione-4,5-dithiolate) and $[Mo_3S_7(ox)_3]^{2-}$ (ox = oxalate)), et démontré leur efficacité pour la réduction des protons en H_2 dans des conditions d'électrocatalyse hétérogène. Ces deux complexes ont été préparés selon des protocoles robustes et caractérisés par diffraction des rayons X (monocristal et poudre) et analyse thermogravimétrique (TGA). Les électrodes ont été modifiées par dépôt d'encres catalytiques constituées principalement de complexes et de noir de carbone. Les résultats montrent que l'activité HER dépend de la composition de l'encre comme la nature du solvant, le rapport catalyseur/carbone ou éventuellement la présence de Nafion®. Il a d'abord été montré que la phase catalytique à base de complexe $[Mo_3S_7(dmit)_3]^{2-}$ présentait une activité remarquablement stable sur une période de 17h, alors que celle à base de $[Mo_3S_7(ox)_3]^{2-}$ se désactive progressivement bien que son activité initiale soit la plus élevée. Cette désactivation peut être le résultat de la réduction électrochimique du complexe survenant avant même la réduction des protons ou de la désorption du catalyseur de la surface de l'électrode. En résumé, cette étude révèle le potentiel de ces clusters thiomolybdiques et met en évidence le rôle modulateur du ligand sur l'activité catalytique et la stabilité des électrodes.

Table of Contents

Introduction

1. Context

1.1 Sustainable H_2 Production by Electrolysis

Hydrogen (H_2) is regarded as key to transitioning into a sustainable, decarbonized, climate-neutral energy system. It is identified as a cleaner alternative to fossil fuels due to its non-toxicity, high gravimetric energy density, and zero-carbon emission. Not only is it useful as fuel that can be converted directly into electricity, but it can also be adopted as an energy vector into which excess energy harvested from renewables can be stored. In addition, it is also widely utilized in the industry as a chemical feedstock for petrochemical refinement, and the synthesis of NH_3 and methanol. Unfortunately, H_2 production is non-trivial, and with the continuous rise in the H_2 demand, it becomes a huge barrier in the implementation of a decarbonized system[1].

Based on the 2020 report of the International Energy Agency, a vast majority of H_2 produced globally comes from non-renewable fossil fuel sources (59% from natural gas, 29% from coal). Moreover, steam reformation, which contributes significant quantities of CO_2 emission, remains the predominant method for H_2 production. Indeed, the same report revealed that the fossil fuel-based hydrogen production accounts for 2.5% of global CO_2 emission from the energy and industry sector in 2020.[2] Water splitting by electrolysis is considered a viable and cleaner means of producing hydrogen as it only requires electricity and water as input. With this method, H_2 is generated in high purity with much lower greenhouse gas footprint. Furthermore, the process can be made 'green' by using only renewable electricity generated by solar and wind power sources (**Figure 1**)[3].

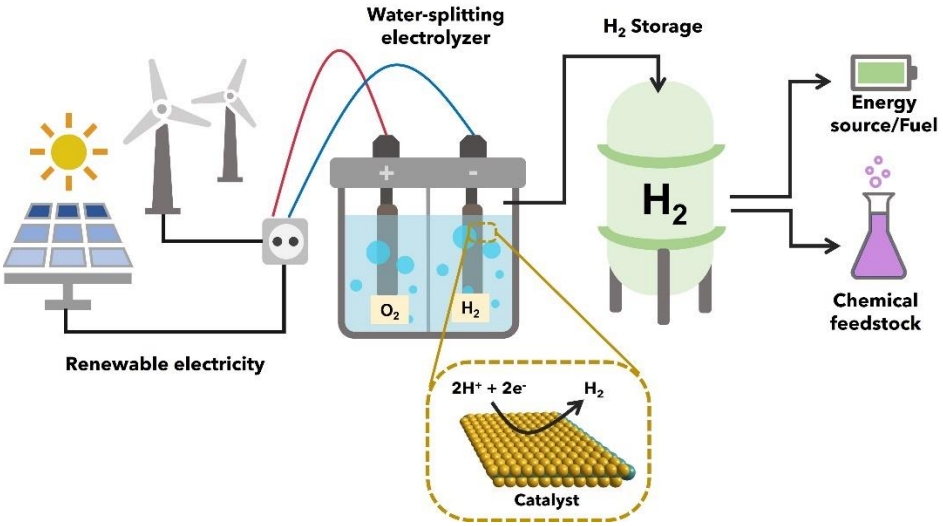

Figure 1. Schematic representation of green H_2 production by electrolysis using solar- and wind-generated electricity.

The operation of water splitting electrolyzers is divided into two half-reactions – the hydrogen evolution reaction (HER: $2\ H^+ + 2\ e^- \rightleftharpoons H_2$) and the oxygen evolution reaction (OER: $2\ H_2O \rightleftharpoons O_2 + 4\ H^+ + 4\ e^-$). Electrolyzers rely on the critical role of electrocatalysts in facilitating both HER and OER. These catalysts lower the kinetic barrier, or overpotential, of these electron transfer processes to minimize the energy input required to drive the reactions[4]. Thus far, Pt remains the best-known catalyst for HER under acidic conditions with almost negligible overpotential. The excellent catalytic properties of Pt has made it a typical cathode material for proton exchange membrane (PEM) electrolyzers, but its scarcity and high cost limits the economic viability of this technology for large-scale commercial applications[5]. While non-noble metal alternatives exist such as Ni, its utility is restricted only in alkaline conditions as low pH promotes its corrosion. This, therefore, opens a challenge of developing low-cost, efficient and robust

electrocatalysts with HER activities that contend with that of Pt to ultimately lead the advancement of water-splitting technologies for sustainable H_2 production.

1.2 Electrocatalytic HER: Mechanism and Evaluation Metrics

Under acidic conditions, HER is believed to proceed via three elementary steps as summarized in **Figure 2**. The first step (Volmer reaction) is the reductive adsorption of proton on the catalyst's active site, followed by the evolution of H_2 either through a proton coupled electron transfer (Heyrovsky reaction) or through the association of two adsorbed H atoms (Tafel reaction). The dependence of these pathways on the adsorption of hydrogen implies the strong influence of the free energy of hydrogen binding, ΔG_{H^*}, on the rate of the overall reaction. This is evident on the volcano plot that results from plotting the catalytic activity as a function of ΔG_{H^*} (**Figure 3**). This volcano relationship follows Sabatier's principle which suggests that the ideal HER catalyst neither binds the intermediate H* too weakly nor too strongly ($\Delta G_{H^*} \approx 0$)[6,7]. In other words, to achieve a more efficient HER catalysis, materials with moderate ΔG_{H^*} must be utilized. Thus, to have substitutes for the precious metals at the top of the volcano (Pt, Pd, and Ir), the intrinsic activity of non-noble metal catalysts can be enhanced by employing strategies that optimize their hydrogen binding energy.

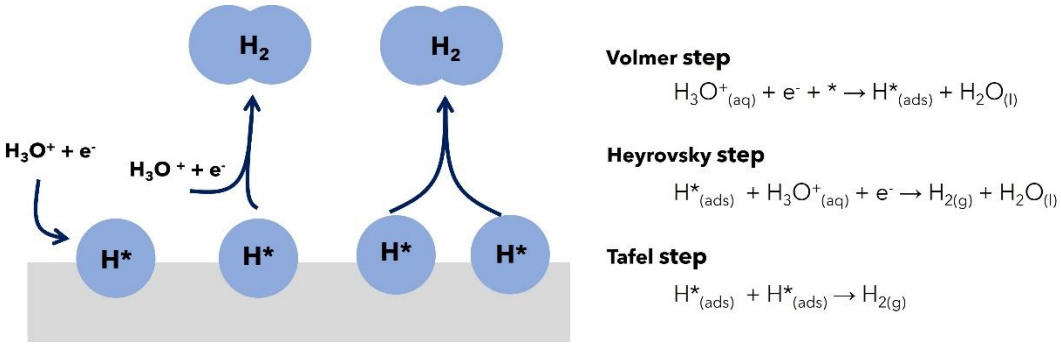

Figure 2. Schematic representation of the three elementary steps of HER in acidic media (* denotes an active site on the catalyst surface).

Evaluating electrocatalytic performance is based on parameters such as overpotential, Tafel slope, exchange current density, electrochemically active surface area (ECSA), Faradaic efficiency, stability, and turnover frequency (TOF).

The rate of an electrochemical reaction is described by an exponential function of the overpotential which can be simplified into a linear form called the Tafel equation (**Equation 1**), where j is the current density (mA cm^{-2}), j_o is the exchange current density, β is the Tafel slope (mV dec^{-1}), and η is the overpotential (mV).

$$\eta = \pm\beta \log|j| \mp \beta \log|j_0| \qquad (1)$$

The overpotential, η, represents the kinetic barrier that must be overcome to drive either the reduction or oxidation process. Usually, the metric used to compare the activities of different catalysts is the overpotential value required to achieve a fixed current density of j = 10 mA cm^{-2}, that is, the current density corresponding to a 12.3% efficient solar-to-hydrogen device[8].

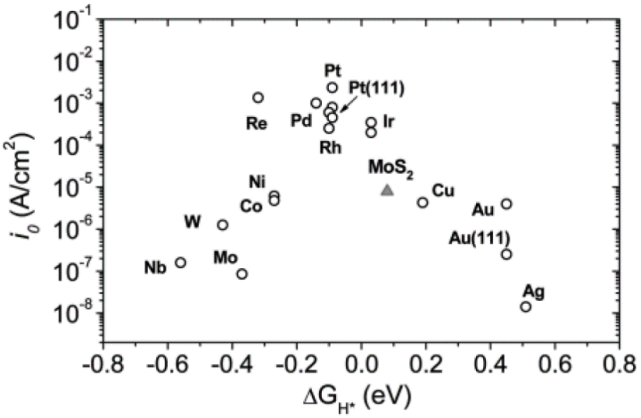

Figure 3. Volcano plot comparing the HER activities of various catalysts in terms of exchange current density as a function of the hydrogen binding free energy, ΔG_{H^*}.[7]

Two other useful parameters that can be derived from the Tafel equation, are the Tafel slope and the exchange current density. The Tafel slope, often expressed in mV per decade (mV dec^{-1}), is determined by several factors such as reaction mechanism and mass transport conditions, but from a practical viewpoint, it can indicate the magnitude of the additional voltage necessary to raise the catalytic current. The exchange current density, on the other hand, measures the intrinsic rate of charge transfer under equilibrium conditions ($\eta = 0$). A high exchange current density, a low Tafel slope, and a low overpotential for a given current density are the hallmarks of a good electrocatalyst.[4,6,8]

Typically, normalization of activities based on mass loading or geometric surface area have been widely adopted for comparing materials. However, these techniques are not suitable due to their inconsistencies that arise from the variation of the surface morphology. Instead, measuring the number of electrocatalytic active sites in terms of ECSA is a preferred approach for assessing the intrinsic activity. Determination of the ECSA involves the estimation of the double-layer capacitance from the measurement of the capacitive current by voltammetry at differential sweep rates in the non-Faradaic potential region. Comparison of the double-layer capacitance with the material's specific capacitance then gives ECSA.[10]

The TOF which describes the number of H_2 evolved per catalytic site per unit time is also a critical metric for catalyst efficiency. Nevertheless, it is practically challenging to accurately measure TOF especially in heterogeneous systems and thus, reported TOFs are taken as average over many sites. Additionally, one can also determine the Faradaic efficiency which is obtained from the ratio of the actual quantity of H_2 detected and the theoretical amount expected from the charge input (**Equation 2**).[4, 9, 10]

$$\text{Faradaic efficiency} = \text{mol } H_2 \text{ produced} \times \frac{nF}{Q} \times 100\% \qquad (2)$$

Finally, examining the stability is also crucial as high durability of the material is a necessary requirement to be integrated as a component of water-splitting devices. To evaluate the stability, potential cycling (100 or 1000 times) by voltametric methods, chronopotentiometry, and chronoamperometric electrolysis are straightforward means that can be adopted.[9]

1.3 Thiomolybdate Clusters as Molecular Electrocatalysts for H_2 Production

Although Pt is the ideal catalyst for the HER due to its exceptional efficiency, its low abundance and high cost has driven the efforts to find and develop replacements that are more suitable for upscaling industrial H_2 production. Among the candidate materials, molybdenum sulfides (MoS_x) are identified as a promising alternative with many studies demonstrating their excellent HER activity, stability in acidic media, and low cost (2500 times cheaper than Pt)[4,5,6,8].

The reactivity of bulk molybdenum disulfide (MoS_2) with H_2 is not unfamiliar as it has been exploited as a catalyst for the hydrodesulfurization (HDS) of crude petroleum[11]. The renewed interest of MoS_x for HER catalysis was prompted by the DFT studies by Hinneman et al. (2005) which revealed that the Mo edges are the HER reaction sites (with ΔG_{H^*} close to zero) while the basal planes are catalytically inactive[25]. This understanding has inspired various strategies to improve the electrocatalytic activity of MoS_x either by nanostructuring to expose greater number of edge sites or by surface doping to tune the hydrogen adsorption strength.

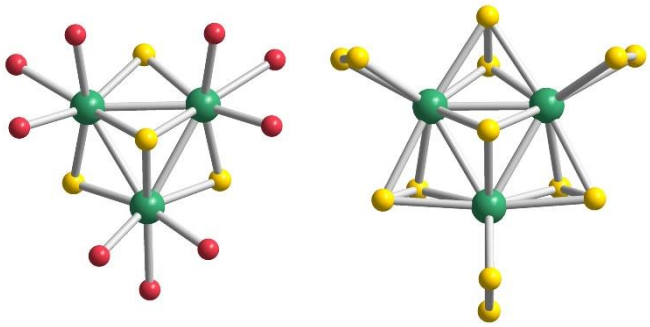

Figure 4. Structural models of trinuclear {Mo_3} clusters of $[Mo_3S_4(H_2O)_9]^{4+}$ (*left*) and $[Mo_3S_{13}]^{2-}$ (*right*). Color code: green = Mo, yellow = S, red = H_2O

Currently existing MoS_x-based catalysts in literature can be broadly classified into crystalline and amorphous materials and discrete clusters[8]. In this work, thiomolybdate molecular clusters will be the main focal point. Molecular clusters of MoS_x with structural motifs that mimic the active sites found in MoS_2 present the advantage of maximizing the density of reactive centers leading to enhanced activity. Indeed, a biomimetic incomplete cubane-type $[Mo_3S_4]^{4+}$ (**Figure 4**) that emulates the metallic active sites of nitrogenase and hydrogenase enzymes was demonstrated to exhibit HER activity (TON = 0.07 s^{-1}) comparable to that of MoS_2 edge surface sites. When sub-monolayer of $[Mo_3S_4]^{4+}$ is supported on a highly orientated pyrolytic graphite (HOPG), a j_o of $2.2 \times 10^{-7}/cm^2$ and a Tafel slope of 120 mV/dec were obtained. However, desorption of the hydrophilic cluster occurs leading to the deterioration of activity with successive potential cycling[12]. Meanwhile, investigation of the trinuclear $[Mo_3S_{13}]^{2-}$ nanoclusters drop-cast on an anodized HOPG revealed excellent HER catalytic activity with overpotentials of only 0.18-0.22 V_{RHE} and a Tafel slope of 57 mV dec^{-1}. Furthermore, the cluster exhibited stability in an acidic condition after 1000 potential sweep cycles, and a higher TOF of 3 s^{-1} (per Mo) outperforming other MoS_x catalysts prepared by wet-chemical methods[8, 13]. The high activity was believed to originate from the inherent high number of S atoms exposed, and evidence indicates the role of the bridging S atoms as active sites[14]. Altogether, these reports illustrate the potential of cluster-type catalysts for H_2 evolution that can be further maximized by modifying the structure either by changing the ligands or by introducing a heterometal. Moreover, this also opens an opportunity to use these molecular counterparts as models for better understanding the mechanism of HER catalysis by MoS_x.

1.4 The ANR THIOMOF Project: Prospect of a Thiomolybdate Cluster-Based Coordination Polymer

Metal-organic frameworks (MOFs) are a class of hybrid materials which present a promising platform for efficient energy conversion systems. MOFs are highly crystalline and porous materials possessing diverse structures that can be tailored by judicious selection of the metal-based nodes and multitopic organic ligands, and implementation of appropriate synthetic conditions (**Figure 5A**). The inherent porosity of MOFs is an advantageous feature for applications in efficient energy conversion because it enables facile mass transport and enhanced kinetics by virtue of the greater number of accessible active sites[15]. A major drawback of majority of MOFs, however, is their poor conductivity due to the ionic nature of the bond between the metal ions and the donor sites of the ligand that are usually N or O.

Charge delocalization and large band dispersion are essential attributes that confer good conductivity. In MOF design, these can be achieved by increasing the spatial and energetic overlap between the orbitals of the metal and those of the organic linker[16,17]. Furthermore, conductivity can be imparted to MOFs by providing different pathways that facilitate charge transport. Through-bond conduction (**Figure 5B**) is enabled by incorporating conjugated organic ligands and metal ions with loosely bound electrons as well as by having highly covalent bonds like metal-sulfur bonds. Additionally, conductive MOFs can be designed using organic ligands that interact through π-π stacking to permit through-space charge transport.[17]

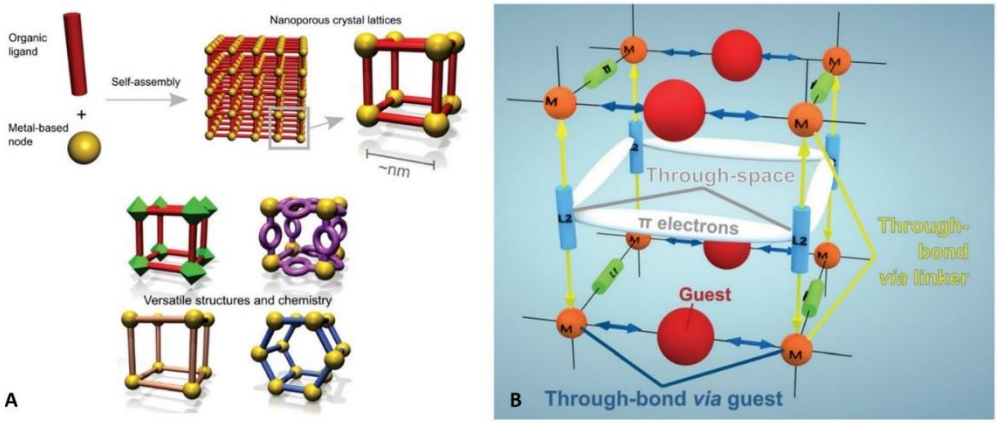

Figure 5. Graphical representation of the (A) formation of diverse MOF structures from the self-assembly of metal nodes and organic ligands, and (B) the three pathways of charge transport in MOFs.[16]

The THIOMOFS project (2020-2024) funded by the Agence Nationale de la Recherce (ANR) was conceived through the collaboration of four French research institutions – Institut Lavoisier de Versailles (ILV), Institut des Matériaux Jean Rouxel de Nantes (IMN), Institut des Sciences Chimiques de Rennes (ISCR) and Institut Charles Gerhardt Montpellier (ICGM) – under the direction of Dr. Thomas Devic (IMN). This project aims to develop three-dimensional multi-redox hybrid frameworks that display both porosity and electronic conductivity for possible application as electrocatalysts or as electrode materials in ion batteries. To tackle the poor conductivity of MOFs, the strategy envisioned by the project involves the reinforcement of through-bond charge conduction by combining metal centers with multiple accessible redox states and polytopic non-innocent dithiolene ligands.

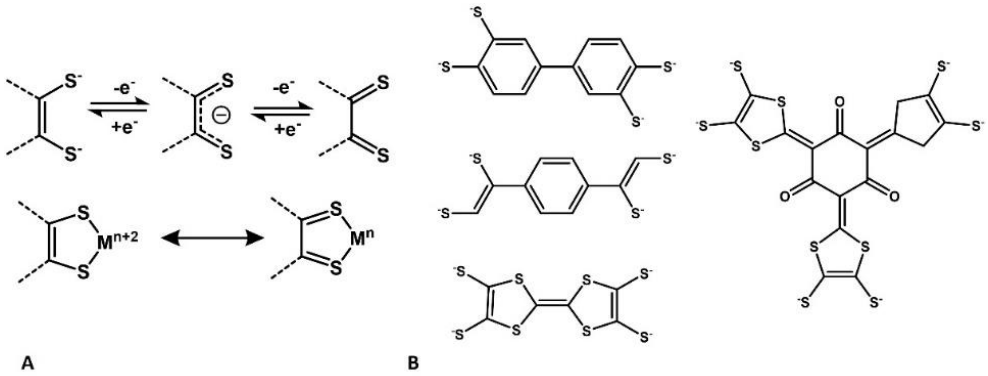

Figure 6. (A) Scheme of the redox states of the dithiolene group (*top*) and the resonant forms of the metal-dithiolene complex (bottom. (B) The bis(dithiolene) and tris(dithiolene) linkers intended to be utilized in the ANR THIOMOFS project.

The choice of polytopic dithiolene linkers (**Figure 6B)** in the construction of conductive MOFs is rationalized by the presence of S donor atoms that provide more covalent character in the metal-ligand bonds. Furthermore, due to the non-innocent nature of dithiolene ligands, they display redox activity and form metal complexes with extensive ligand-metal orbital mixing resulting in ambiguous oxidation state

assignment (**Figure 6A**)[18]. When incorporated as building units of coordination networks, metal-dithiolene complexes can permit long-range electron delocalization that is prerequisite to electronic conductivity.

One aspect being explored in the THIOMOFS project is the incorporation of thiomolybdate clusters as secondary building units (SBUs) to imbue the extended network with HER activity. Recently, dimers and a chain based on $\{Mo_3S_7\}$ cluster units connected by ditopic benzenedithiol linkers have been synthesized by facile ligand substitution chemistry. Indeed, the extended chain of the trinuclear cluster was found to exhibit HER activity with comparable durability to that of $[Mo_3S_{13}]^{2-}$ and with an overpotential of 89 mV.[18] To date, however, MOFs or coordination polymers combining thiomolybdate cluster SBUs with non-innocent dithiolene linkers have not yet been explored. Such hybrid material, if successfully realized, can offer a unique and desirable mix of electrocatalytic activity and conductivity.

2. Objectives and Scope of the Thesis

A requisite for the development of coordination polymers based on thiomolybdate cluster and dithiolene linkers is the knowledge of the stability and activity of the building units and the appropriate synthetic conditions to control the kinetics and the yield of the reaction. For this purpose, studying a molecular model system built from 1,3-dithia-2-thione-4,5-dithiolate ligand (dmit) coordinated to the trinuclear core $[Mo_3S_7]^{4+}$ can serve as a starting point.

Ben Hamouda H., a former Master's student at ILV has successfully synthesized and structurally characterized the $[Mo_3S_7(dmit)_3]^{2-}$ complex (**Figure 7**). Kinetic studies of the transmetalation reaction between the $[Mo_3S_7Cl_6]^{2-}$ precursor and the $(dmit)SnBu_2$ proligand in solution by UV-Vis spectroscopy has demonstrated the temperature-dependence of the rate and its inhibition in the presence of halide ions. These results provide important means of modulating the reaction rate towards the preparation of crystalline MOFs based on thiomolybdate cluster and dithiolene.

Building on the work of Ben Hamouda, H. and in line with the objectives of the ANR THIOMOFS project, here we aim to further characterize $[Mo_3S_7(dmit)_3]^{2-}$ and evaluate its HER activity. Furthermore, to gain insight on the influence of the ligand, we also explored the synthesis of $[Mo_3S_7(ox)_3]^{2-}$ (ox = oxalate ion) (**Figure 7**) and compared its electrochemical properties and electrocatalytic activity with the former.

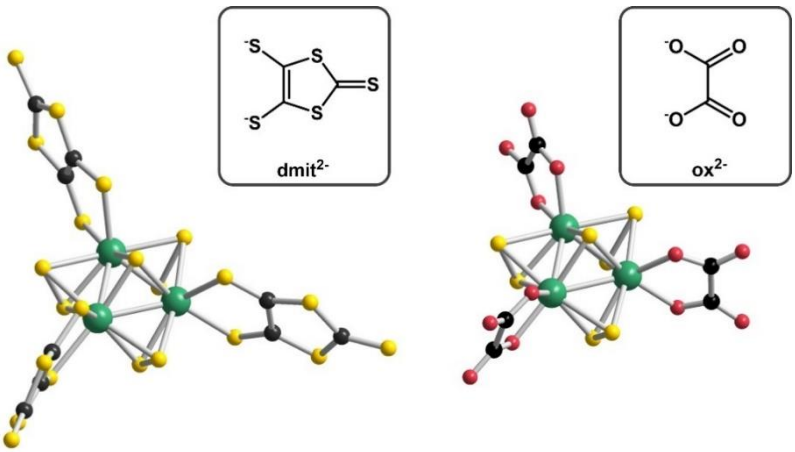

Figure 7. Structural models of the thiomolybdate $\{Mo_3S_7\}$ cluster complexes under study: $[Mo_3S_7(dmit)_3]^{2-}$ (*left*) and $[Mo_3S_7(ox)_3]^{2-}$ (*right*). Color code: green = Mo, yellow = S, red = O, black = C

Materials and Methods

1. Synthesis

Preparation of $(NH_4)_2[Mo_3S_{13}]\cdot 2H_2O$. In 300 mL of aqueous solution of 28% NH_3 (Alfa Aesar) (d = 0.90), 40 g (32 mmol) of $(NH_4)_6Mo_7O_{24}\cdot 4H_2O$ (Alfa Aesar) was dissolved until a clear solution was obtained. With continuous stirring, a continuous flow of H_2S gas was introduced into the flask until the point of saturation was reached. A color change was observed from yellow to orange and then deep red. The sulfurization reaction was stopped after 30 mins and the appearance of red crystals of $(NH_4)_2[MoS_4]$ was observed. To this, 20 g (78 mmol) of elemental sulfur (S_8, Acros Organics) was added and the resulting mixture was heated to boiling under reflux for 20 h. Dark red crystalline powder of $(NH_4)_2[Mo_3S_{13}]\cdot 2H_2O$ were formed and were collected by filtration through a glass frit followed by successive washes of water, ethanol, and diethyl ether before drying.

Molar mass: 776 g/mol *Yield:* 41.5 g (53.4 mmol, 72% based on Mo)

Characteristic IR bands (in cm^{-1}): 1390 (m, δ(N-H)), 540 (s, $\nu(S\text{-}S)_{bridge}$), 503 (s, $\nu(S\text{-}S)_{terminal}$), 459 (w, $\nu(Mo\text{-}(\mu_3\text{-}S))$)

Preparation of $A_2[Mo_3S_7Cl_6]\cdot nH_2O$ ($A = NH_4^+$, n = 6; $A = NBu_4^+$, n = 0). A solution of 30 g (38.6 mmol) $(NH_4)_2[Mo_3S_{13}]\cdot 2H_2O$ in 300 mL 37% HCl (Carlo Erba Reagents) was heated to boiling under reflux for 1 h with continuous stirring. The color of the mixture was observed to develop from burgundy red to brownish orange. The brown solid by-product (mostly elemental sulfur) was separated by hot filtration and the dark colored filtrate was left to stand at room temperature for days to allow the growth of orange crystals of $(NH_4)_2[Mo_3S_7Cl_6]\cdot 6H_2O$. The crystals were separated by filtration and then air dried.

Molar mass: 869 g/mol *Yield:* 17.0 g (19.6 mmol, 51%).

Characteristic IR bands (in cm^{-1}): 1390 (s, δ(N-H)), 560 (s, $\nu(S\text{-}S)_{bridge}$), 460 (w, $\nu(Mo\text{-}(\mu_3\text{-}S))$)

The NBu_4^+ salt of $[Mo_3S_7Cl_6]^{2-}$ was prepared by adding 1.5 g (5.4 mmol) of NBu_4Cl (Sigma-Aldrich) to a solution of 2.0 g (2.3 mmol) $(NH_4)_2[Mo_3S_7Cl_6]\cdot 6H_2O$ in 40 mL 6 M HCl. The orange precipitate was filtered and then air dried. Yield: 2.7 g (2.23 mmol, 97%)

Molar mass: 1210 g/mol

Characteristic IR bands (in cm^{-1}): 2950 (s, $\nu(sp^3C\text{-}H)$, 2870 (s, $\nu(sp^3C\text{-}H)$, 1470 (s, δ(C-H)), 1380 (m, δ(C-H)), 560 (s, $\nu(S\text{-}S)_{bridge}$), 460 (w, $\nu(Mo\text{-}(\mu_3\text{-}S))$)

Preparation of $K_5\{[Mo_3S_7(ox)_3]_2\cdot Cl\}\cdot 9.75H_2O$ and $Cs_4[Mo_3S_7(ox)_3]_2\cdot H_2C_2O_4\cdot 11H_2O$. With continuous stirring, 1.75 g (2.0 mmol) $(NH_4)_2[Mo_3S_7Cl_6]\cdot 6H_2O$ was slowly added into a warm solution of 1.34 g (5.3 eq, 10.6 mmol) oxalic acid dihydrate ($H_2ox\cdot 2H_2O$) in 75 mL water. The mixture was heated until a clear red solution was obtained. Addition of excess KCl (8 g, 0.107 mol or CsCl (28 g, 0.167 mol) and cooling of the resulting solution in an ice bath led to the generation of red-orange needle-shaped crystals of alkali metal salts $A_2[Mo_3S_7(ox)_3]$. The product was collected by filtration, washed with water, and air dried.

Molar mass: $K_5\{[Mo_3S_7(ox)_3]_2\cdot Cl\}\cdot 9.75H_2O$ – 1959 g/mol

Yield: 1.8 g (0.92 mmol, 92% based on Mo)

Molar mass: $Cs_4[Mo_3S_7(ox)_3]_2\cdot H_2C_2O_4\cdot 11H_2O$ - 2372 g/mol

Yield: 0.54 g (0.23 mmol, 79% based on Mo from 1.15 mmol $(NH_4)_2[Mo_3S_7Cl_6]\cdot 6H_2O$)

Characteristic IR bands (in cm^{-1}): 1700 (s, ν(C=O)), 1370 (s, ν(C-O) + ν (C-C)), 905 (m, ν (C-O) + δ(O-C-O)), 790 (m, δ(O-C-O) + ν (M-O)), 540 (w, ν(Mo-O)), 470 (w, ν(Mo – (μ3-S)))

Preparation of $(NBu_4)_2[Mo_3S_7(dmit)_3]$. An orange solution of $(NBu_4)_2[Mo_3S_7Cl_6]$ (100 mg, 0.083 mmol) in 60 mL of degassed acetonitrile (by argon bubbling) was reacted with (*n*-Bu)$_2$Sn(dmit) (106 mg,0.247 mmol) with heating under reflux for 1 h with continuous stirring. An immediate color change of the mixture from orange to dark red and then eventually to dark violet was observed. The solution was dried *in vacuo* until the volume was reduced to about less than 20% of the initial. The (*n*-Bu)$_2$SnCl$_2$ byproduct was removed by adding 50 mL of diethyl ether to the residue and then filtering the mixture to separate the dark violet precipitate from the diethyl ether solution. The precipitate was treated with excessive volume of CH_2Cl_2 to dissolve and recover the entire product. Addition of diethyl ether to the CH_2Cl_2 solution to give a mixture of CH_2Cl_2/diethyl ether (13 mL/4 mL) yields dark violet needle crystals of $(NBu_4)_2[Mo_3S_7(dmit)_3]$ by slow evaporation.

Molar mass: 1586 g/mol *Yield:* 54-87 mg (0.034-0.055 mmol, 41-66%)

Characteristic IR bands (in cm^{-1}): 2940 (s, ν(*sp*^{3}C-H)), 2860 (s, ν(*sp*^{3}C-H)), 1440 (s, ν(C = C)), 1040 (s, ν(C = C)), 555 (w, ν(S-S)$_{bridge}$), 510 (m, ν(Mo-S$_{dmit}$)), 450 (m, ν(Mo – (μ3-S)))

2. Physical Characterization

Single crystal X-ray diffraction (XRD). X-ray diffraction intensities for $(NBu_4)_2[Mo_3S_7(dmit)_3]$, $K_5\{[Mo_3S_7(ox)_3]_2\cdot Cl\}\cdot 9.75H_2O$, and $Cs_4[Mo_3S_7(ox)_3]\cdot H_2C_2O_4\cdot 11H_2O$ were collected at T = 220 K using a Bruker D8 VENTURE diffractometer equipped with a PHOTON 100 CMOS bidimensional detector using X-ray Mo Kα monochromatic radiation (λ = 0.71073 Å).

Fourier-transform infrared (FT-IR) spectroscopy. FT-IR spectra were recorded in transmission mode from 4000-400 cm^{-1} with a resolution of 4 cm^{-1} on a 6700 FT-IR Nicolet spectrometer equipped with a diamond attenuated total reflection (ATR) accessory for sampling.

Powder X-ray diffraction (PXRD). The diffractograms were recorded using Siemens D500 diffractometer with CuKα radiation (λ = 1.5406 Å) operating in Bragg-Brentano configuration in the range 2θ = 5-45° with a step length of 0.02°.

Thermogravimetric analysis (TGA). Thermogravimetric analyses were performed on a Mettler Toledo TGA/DSC 3, STAR^e System instrument under oxygen flow (40 mL min^{-1}) from room temperature up to 700°C at a rate of 5°C min^{-1}. The gas released during heating was monitored by coupling the instrument to a Thermo Scientific™ Nicolet iS10 FTIR spectrometer. The infrared spectra collected were compared with a library for identification.

Scanning electron microscopy with energy dispersive X-ray spectroscopy (SEM-EDS). The SEM micrographs were obtained using a SEM-FEG (Scanning Electron Microscope enhanced by a Field Emission Gun) equipment (JSM 7001-F, Jeol) at 15 kV and 10 mm working distance. EDS measurements were then acquired with a SDD XMax 50 mm^2 detector and the Aztec (Oxford) system using the same experimental conditions. The quantification was performed using Lα lines and based on the standard library provided by the manufacturer.

3. Electrochemical Measurements

Preparation of the modified working electrode. The glassy carbon (GC) electrode (Ø = 3.0 mm, A = 0.071 cm^2) was polished to a mirror finish using an aqueous slurry of alumina powder on a silk polishing cloth (Struers DP-Dur). The catalytic inks were composed of a mixture of catalyst, carbon powder (Vulcan XC-72R) and solvent (either methanol, CH_2Cl_2, or DMF). To examine the effect of the catalyst/ carbon ratio, the solvent, and the presence of Nafion® (Sigma-Aldrich) on the activity, the amounts of the

components were varied as summarized in **Table 1**. The ink suspensions were homogenized by sonication for 30 mins and using a micropipette, 4-8 µL inks were drop-casted on the GC electrode surface. The modified electrodes were left to dry before testing.

Table 1. List of the composition and quantities of the components of the catalytic inks prepared.

	mass of the catalyst (mole)	mass of carbon	solvent (volume)	Nafion® (volume)
$(NBu_4)_2[Mo_3S_7(dmit)_3]$	3 mg	---	CH_2Cl_2 (200 µL)	(-)
	6 mg	3 mg	CH_2Cl_2 (400 µL)	(-)
	5 mg	10 mg	CH_2Cl_2 (340 µL)	(-)
	3 mg	10 mg	CH_2Cl_2 (200 µL)	(-)
	3 mg	10 mg	DMF (200 µL)	(-)
	3 mg	10 mg	DMF (150 µL)	(+) (50 µL)
$K_5\{[Mo_3S_7(ox)_3]_2 \cdot Cl\} \cdot 9.75H_2O$	6 mg	3 mg	CH_2Cl_2 (400 µL)	(-)
	6 mg	3 mg	MeOH (400 µL)	(-)
	6 mg	3 mg	DMF (400 µL)	(-)
	6 mg	3 mg	DMF (300 µL)	(+) (100 µL)
$(NBu_4)_2[Mo_3S_7(ox)_3]$	6 mg	3 mg	DMF (400 µL)	(-)
	6 mg	3 mg	DMF (300 µL)	(-)
	6 mg	3 mg	MeOH (400 µL)	(-)
	4.8 mg	2.4 mg	MeOH (400 µL)	(-)

HER activity measurements. The electrochemical measurements were carried out in a conventional three-electrode electrochemical cell using a PalmSens4 potentiostat. The GC electrode modified with different catalytic inks served as the working electrode with graphite rod as counter electrode and a Ag|AgCl (saturated KCl) as reference electrode. Impedance measurement was done to estimate the electrolyte resistance *R* of the cell for Ohmic drop correction of the potentials.

The electrochemical HER performance was studied by linear sweep voltammetry (LSV) with a scan rate of 5 mV s^{-1} with the working electrode rotating at 2500 rpm in 50mL 0.5 M H_2SO_4. The electrolyte solutions were de-aerated for 30 minutes by Ar bubbling and an Ar atmosphere was maintained over the solution to prevent air contamination. The potentials were converted to the reference hydrogen electrode (RHE) scale using **Equation 3**:

$$E_{RHE} = E_{Ag|AgCl} + 0.197\ V + 0.059\ V\ pH - iR \qquad (3)$$

The LSV polarization curves were obtained by plotting the current density, j (mA cm^{-2}), versus E_{RHE} (V) where j is given by dividing the measured current, i (mA), by the geometric area (cm^2) of the GC electrode. The Tafel slopes were determined from the plot of the overpotential, $\eta = E_{RHE} - 0$, against $\log|j|$ (**Equation 1**).

Cyclic voltammetry (CV) measurements. The cyclic voltammetry (CV) study of the redox behavior of $Cs_4[Mo_3S_7(ox)_3]_2 \cdot H_2C_2O_4 \cdot 11H_2O$ was performed using a three-electrode electrochemical cell consisting of a polished GC working electrode, a Pt plate counter electrode, and a Ag|AgCl (saturated KCl) reference electrode. The measurements were obtained by applying a potential sweep between -0.5 to 0 $V_{Ag|AgCl}$ at a scan rate of 50 mV s^{-1}

To investigate the influence of the pH on the reduction potential, E_c, of the complex, voltammetry was done in 30 mL 0.5 M HSO_4^-/SO_4^{2-} buffer solutions with pH of 1.0, 1.3, and 1.7. The concentration of the complex was also varied (0.14, 0.28, 0.42 mM) at each pH condition by adding incremental amounts of

$Cs_4[Mo_3S_7(ox)_3]\cdot H_2C_2O_4\cdot 11H_2O$. The effect of the presence of H_2ox was also explored by adding increasing amounts of $H_2ox\cdot 2H_2O$ into 0.21 mM $Cs_4[Mo_3S_7(ox)_3]\cdot H_2C_2O_4\cdot 11H_2O$ in 0.5 M HSO_4^-/SO_4^{2-} buffer (pH 1.0), varying the H_2ox concentration from 1.50 to 12.0 mM.

Measurement of H_2 production. An online GC (INFICON Micro GC Fusion®) gas analyzer equipped with a thermal conductivity detector (TCD) connected to an air-tight electrochemical cell was used to quantify the H_2 generated during the electrocatalytic H_2 evolution. The cell was composed of two compartments, one for each of the cathodic and anodic reactions, separated by a glass frit. Electrochemical measurements were done in 0.5 M H_2SO_4 using the modified GC electrode as the rotating working electrode (2500 rpm), a graphite rod as counter electrode, and saturated calomel electrode (SCE) as reference electrode. Prior to measurement, the electrolyte solution was degassed with Ar for at least 30 mins. A constant potential of -0.65 V_{SCE} (≈ -0.39 V_{RHE}) was applied and chronoamperometric measurement was employed for a period of 6 h. A flowing Ar carrier gas is constantly pumped in the cell at a rate of v = 3 L min^{-1} and automated sampling of the headspace occurs every t = 5 minutes. The acquisition of the chromatogram was extended for 3 hours more than the chronoamperometry to ensure that all the H_2 generated are accounted for when calculating the yield. Using the concentration (ppm), c, of the H_2 determined from a chromatogram, the number moles of H_2 was calculated using the following **Equation 4** derived from the ideal gas equation:

$$n_{H_2} = \frac{Pcvt}{1000000RT} = \left(6.13 \times 10^{-7}\ \frac{mol}{ppm}\right) c \qquad \text{at P = 1 atm and T = 298 K} \qquad (4)$$

Assuming the H_2 gas detected comes solely from the electrochemical reaction and two electrons (n = 2) are consumed for every H_2 molecule generated, the Faradaic efficiency can be calculated from the total charge input (C), Q, using **Equation 5**:

$$Faradaic\ yield\ (\%) = n_{H_2} \times \frac{2F}{Q} \times 100\% \qquad (5)$$

Results and Discussion

1. Synthesis and Physical Characterization of the $\{Mo_3S_7\}$ Complexes

1.1 Synthesis of the $[Mo_3S_7Cl_6]^{2-}$ Precursor

In general, the preparation of $\{Mo_3S_7\}$ derivatives can be accessed through the $[Mo_3S_7X_6]^{2-}$ anion (X = Cl, Br) whose labile halides allow for subsequent ligand substitution. The preparation of the $[Mo_3S_7Cl_6]^{2-}$ precursor started with the hydrolysis of $(NH_4)_6Mo_7O_{24}\cdot 4H_2O$ in 28% ammoniacal solution (**Scheme 1**). Direct sulfurization of the solution with H_2S yields the mononuclear Mo^{VI} building block $[MoS_4]^{2-}$. Addition of elemental sulfur to this basic mixture generates anionic polysulfides that then promotes the condensation of $[MoS_4]^{2-}$ molecules with the concomitant reduction of Mo^{VI} to Mo^{IV} to give red wine crystals of $(NH_4)_2Mo_3S_{13}\cdot 2H_2O$. The reaction of $(NH_4)_2Mo_3S_{13}\cdot 2H_2O$ with concentrated HCl under boiling conditions (**Scheme 2**) then leads to the displacement of the three labile terminal S_2^{2-} ligands with six Cl^- ligands producing dark orange crystals of $(NH_4)_2[Mo_3S_7Cl_6]\cdot 6H_2O$. The NBu_4^+ salt of the compound was isolated by precipitating $(NH_4)_2[Mo_3S_7Cl_6]$ from 6M HCl solution with excess NBu_4Cl.

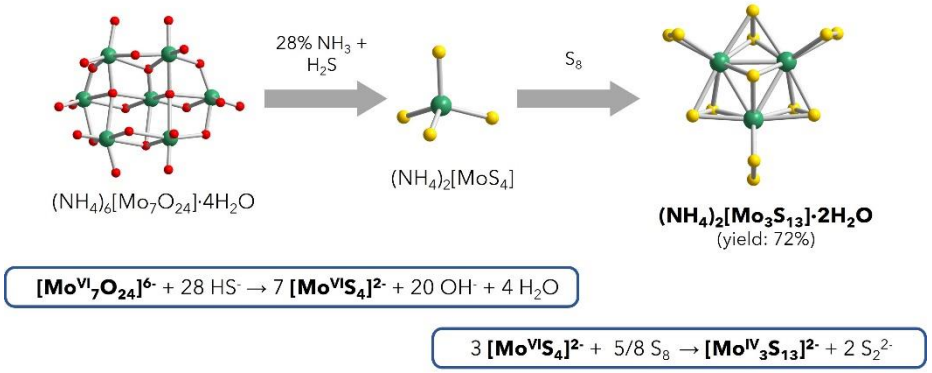

Scheme 1. Synthesis of $[Mo_3S_{13}]^{2-}$ by sulfurization of $[Mo_7O_{24}]^{6-}$ (counterions not shown for clarity)

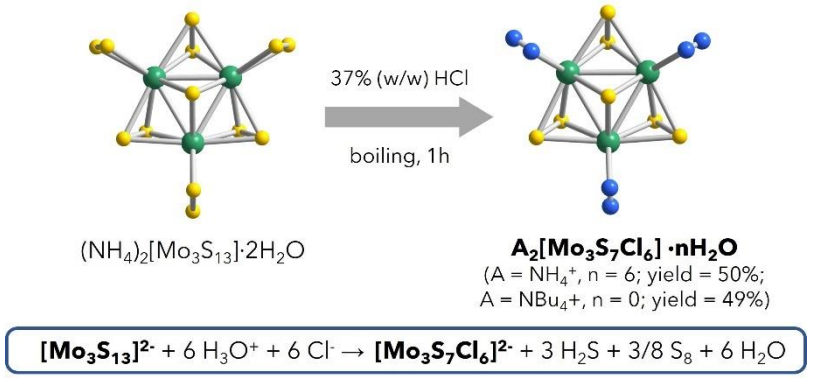

Scheme 2. Synthesis of $[Mo_3S_7Cl_6]^{2-}$ by ligand substitution of terminal S_2^{2-} by Cl^- (counterions not shown for clarity)

1.2 Synthesis of $[Mo_3S_7(dmit)_3]^{2-}$ and $[Mo_3S_7(ox)_3]^{2-}$

The $[Mo_3S_7(dmit)_3]^{2-}$ complex (hereon **$\{Mo_3\}$-dmit**) was synthesized through the direct transmetalation reaction between the $[Mo_3S_7Cl_6]^{2-}$ and dibutyltin-protected dmit in acetonitrile (**Scheme 3**). This approach was pursued because dithiolate tin complexes have been

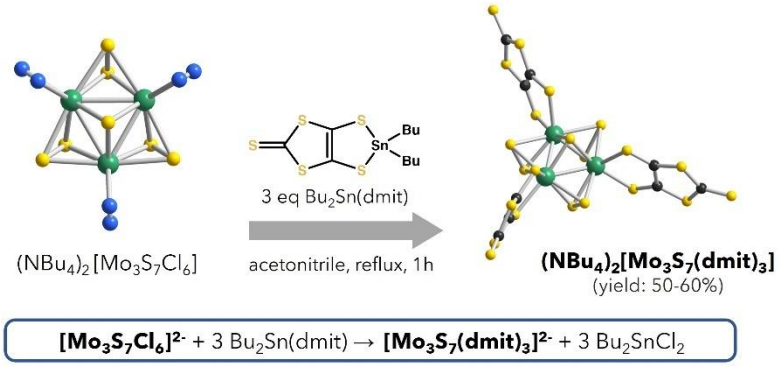

Scheme 3. Preparation of **{Mo$_3$}-dmit** by transmetalation (counterions not shown for clarity)

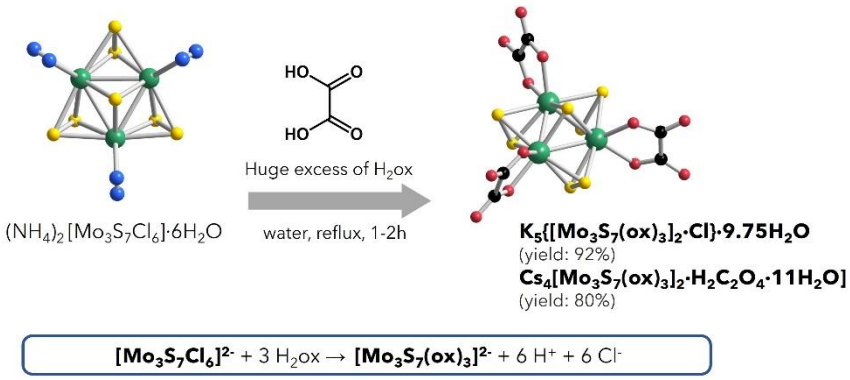

Scheme 4. Preparation of **{Mo$_3$}-ox** by ligand substitution with excess $H_2C_2O_4$ (counterions not shown for clarity)

demonstrated to be good transfer agents. The Bu_2SnCl_2 byproduct can be easily removed by washing with diethyl ether in which the $(NBu_4)_2$**{Mo$_3$}-dmit** is insoluble and precipitates out into intensely dark purple solid. A side reaction that leads to the formation of an unknown product, however, results in low yield (about 50%). Although this product was not further identified, it was presumed to be the neutral $[Mo_3S_7(dmit)_3]^0$ based on the matching FTIR spectra and existing evidence of the facile oxidation of the dianionic species[20].

The transmetalation reaction was accompanied by a transition of color from orange to violet. This is attributed to the shift in the absorption band of the proligand at 440 (ε = 10 500 M^{-1} cm^{-1}) nm to longer wavelengths in the complex at around 500 nm (ε = 37 400 M^{-1} cm^{-1}) (**Figure 8**). The intense electronic absorption arises mainly from LMCT and is an indication of a large π electronic delocalization involving both the dmit ligand and the cluster[20].

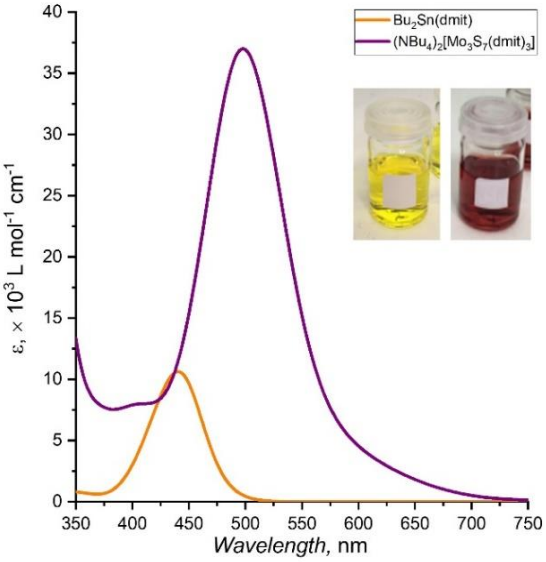

Figure 8. UV-Vis spectra of the proligand $Bu_2Sn(dmit)$ and **{Mo$_3$}-dmit** in acetonitrile and the actual color of their solutions (shown in the inset).

Ligand substitution of the Cl^- ligands of $[Mo_3S_7Cl_6]^{2-}$ upon treatment of excess oxalic acid in aqueous solution under reflux afforded the $[Mo_3S_7(ox)_3]^{2-}$ derivative (hereon **{Mo$_3$}-ox**) (**Scheme 4**). The water-soluble complex was isolated by crystallization with alkali metal chloride salts (K^+, Cs^+) resulting in good to excellent yields (80% for Cs^+ and 92% for K^+). This complex has also been prepared

by solvent-free mechanochemical route[21] but the mild wet chemical approach in aqueous medium gives better yield.

1.3 Structural Features of $[Mo_3S_7(dmit)_3]^{2-}$ and $[Mo_3S_7(ox)_3]^{2-}$

Single crystal XRD data and the length of selected bonds for both the **{Mo_3}-dmit** and **{Mo_3}-ox** are summarized in **Tables 2** and **3**. The core unit of the complexes consists of a trinuclear anionic cluster $\{Mo^{IV}_3\}$ with three Mo centers defining an equilateral triangle. An apical bridging sulfido ligand (μ_3-S^{2-}) caps the trinuclear plane and adjacent Mo atoms are bridged by a disulfido ligand (η^2-μ-S_2^{2-}) resulting in an overall C_{3v} symmetry. The two S atoms of a disulfido bridge are non-equivalent - one is nearly coplanar with the Mo atoms (*equatorial*) while the other lies outside of the plane (*axial*).

In the structure of the **{Mo_3}-dmit** complex, the dithiolene ligands lie almost perpendicular to the trinuclear plane and bend slightly towards the apical S due to the steric strain exerted by the axial S atoms (**Figure 9A**). The two thiolate S atoms of dmit (designated S_{cis} and S_{trans} with respect to the μ_3-S) coordinate asymmetrically with Mo. Because of the bending of dmit, Mo-S_{trans} is slightly longer than Mo-S_{cis} ($\Delta \approx 0.07$ Å).

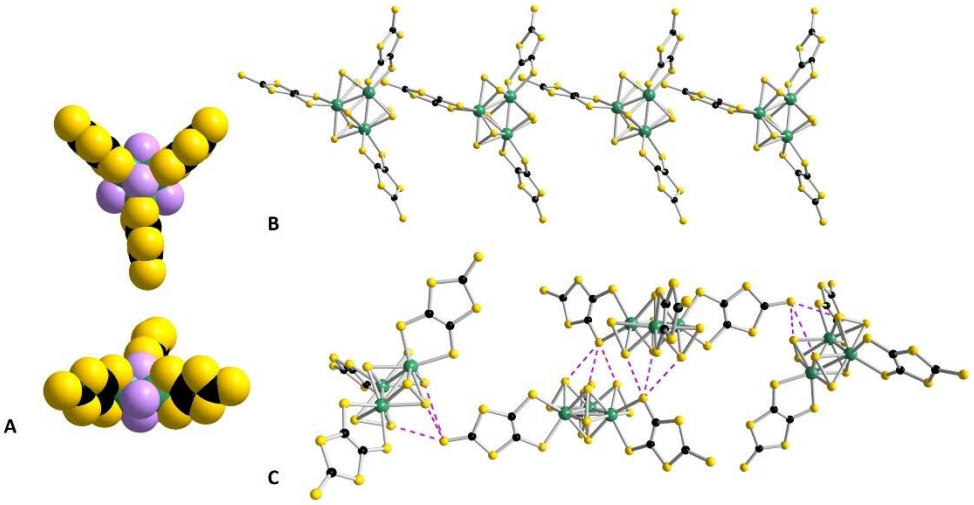

Figure 9. Crystal structure of $(NBu_4)_2$**{Mo_3}-dmit**: (A) space filling model (top- and side-view) of a **{Mo_3}-dmit** molecule (S atoms of the cluster are colored in pink to distinguish from the S atoms of the ligand), (B) packing of the units along the *b* axis, and (C) the S···S interactions (shown as pink ---) between the units on the *ac* plane. Color code: green = Mo, yellow = S, red = O, black = C

A prominent feature apparent in the solid-state structure is the non-covalent interactions between the S atoms of the neighboring molecules. Notably, the electrophilic axial S atoms of the inner cluster can form interactions with either the dithiolate or thione S of a nearby complex (**Figure 9C**). Possible interactions can also arise from the electrophilic endocyclic S. These intermolecular S···S contacts have been associated to the semiconducting property exhibited by the neutral $[Mo_3S_7(dmit)_3]^o$ derivative as reported by Llusar R., et al. (2005)[20].

{Mo_3}-ox has a structure analogous to that of the former. The asymmetric coordination of oxalate also results in Mo-O_{trans} being longer than M-O_{cis} ($\Delta \approx 0.03$ Å). In contrast, however, the **{Mo_3}-ox** units do not exist as discrete species but form a sandwich-like ionic adduct through the association of the Cl^- anion to six electrophilic axial S of two clusters[21] (**Figure 10A**). Whether or not this adduct also exists in the solution phase may be a subject of further investigation, and may be determined by ESI-MS. On a

larger scale, these ionic assemblies associate into a layered arrangement (**Figure 10B)** in which the alkali metal cation K^+ of the K_5(**{Mo_3}-ox**)$_2$Cl·9.75 H_2O salt fills the interlayer space.

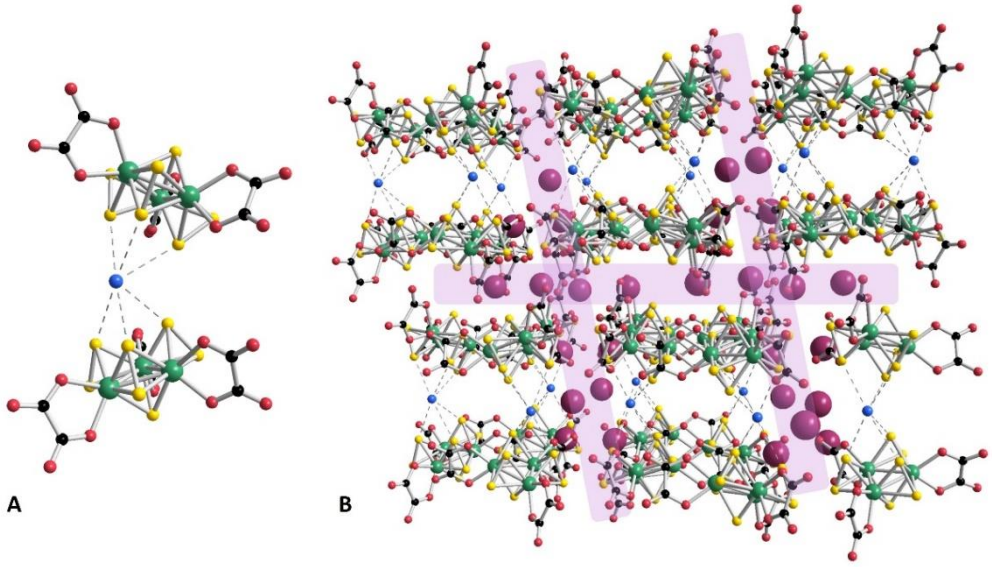

Figure 10. Crystal structure of K_5(**{Mo_3}-ox**)$_2$Cl·9.75 H_2O: (A) formation of a sandwich structure by the ionic triplet [(**{Mo_3}-ox**)$_2$Cl]$^{5-}$ and (B) layered arrangement of the ionic triplets on the *ac* plane with K^+ ions in the interlayer space (highlighted in purple). Color code: green = Mo, yellow = S, red = O, black = C, blue = Cl, purple = K

Table 2. Crystal data for K_5(**{Mo_3}-ox**)$_2$Cl·9.75 H_2O and $(NBu_4)_2$**{Mo_3}-dmit**

	K_5(**{Mo_3}-ox**)$_2$Cl·9.75 H_2O	$(NBu_4)_2$**{Mo_3}-dmit**
Formula	$Mo_{24}S_{56}O_{135}C_{48}K_{20}Cl_4$	$Mo_{48}S_{352}N_{32}C_{532}$
Formula weight, g mol^{-1}	7758.48	22730.4
Crystal system	monoclinic	monoclinic
Space group	*P* 1 21/c 1 (14)	*P* 1 21/c 1 (14)
a, Å	14.8972(5)	19.8494(30)
b, Å	13.2905(4)	20.6855(22)
c, Å	27.0701(8)	65.5796(50)
b, °	101.882(1)°	90.0000°
V, Å^3	5244.81(28)	26926.64(538)
$d_{calc,}$ g cm^{-3}	2.45624	1.40168

Table 3. Selected bond lengths for K_5(**{Mo_3}-ox**)$_2$Cl·9.75 H_2O and $(NBu_4)_2$**{Mo_3}-dmit**

	K_5(**{Mo_3}-ox**)$_2$Cl·9.75 H_2O	$(NBu_4)_2$**{Mo_3}-dmit**
Mo-Mo	2.72	2.77
Mo-μ_3-S	2.37	2.36
Mo- μ_2-S	2.49 (equatorial) 2.40 (axial)	2.52 (equatorial) 2.42 (axial)
Mo-S_{dmit}	----	2.44 (cis) 2.51 (trans)
Mo-$O_{oxalate}$	2.10 (cis) 2.13 (trans)	----

1.4 Bulk Characterization of $[Mo_3S_7(dmit)_3]^{2-}$ and $[Mo_3S_7(ox)_3]^{2-}$ by PXRD and TGA

To check the purity and homogeneity of the products as well as confirm the chemical formula obtained from the single crystal XRD data, bulk characterizations by powder XRD (PXRD) and TGA were performed. The diffractograms in **Figure 11** show that both compounds were synthesized with good crystallinity. Slight broadening of the peaks in the PXRD pattern may have resulted from the variations in the crystal size or the presence of some amorphous phase. Even though the patterns of relative intensities do not completely match, the PXRD peaks are observed in the same angles as those of the peaks predicted by the single crystal XRD data which is indicative of the adequate purity and homogeneity of the products.

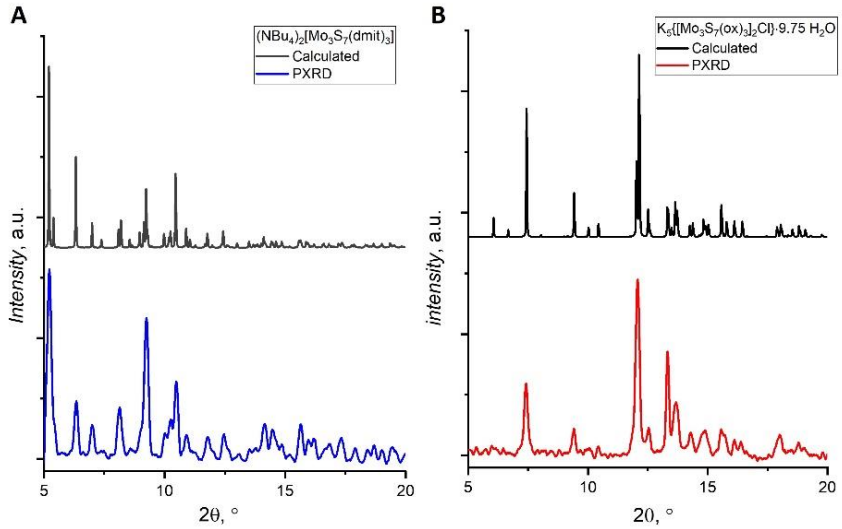

Figure 11. Comparison of the diffractograms obtained from PXRD analysis against the calculation from the single crystal XRD data of $(NBu_4)_2$**{Mo_3}-dmit** (A) and K_5(**{Mo_3}-ox**)$_2$Cl·9.75 H_2O (B)

Both compounds were also subjected to TGA coupled with simultaneous FTIR spectroscopy to identify the gas produced from the thermal decomposition process under O_2 atmosphere. The TG curve of $(NBu_4)_2$**{Mo_3}-dmit** shows a total weight loss of 74% from two stages of thermal degradation between 25-700 °C (**Figure 12A**). The first stage (Δ = 45% *vs* calcd. 43%) occurs between 150-320°C which is associated to the loss of the *dmit* ligands and partial decomposition of the NBu_4^+ counterion based on the detection of CS_2 and H_2O at 200°C by FTIR. Although not visible on the IR spectrum, N is presumed to be released at this point as well in the form of the IR inactive dinitrogen, N_2. This is followed by the complete combustion of NBu_4^+ and the S atoms of the $\{Mo_3S_7\}$ cluster (Δ = 29% vs calcd. 38%) into CO_2, H_2O and SO_2, respectively, in the range of 380-620 °C. SEM-EDS analysis of the white crystalline residue obtained after TGA showed an atomic ratio of 3:0.18 Mo:S (vs 3:7 from formula) indicating that most that had remained was MoO_3. In fact, the remaining 26% from the TG curve corresponds to the % weight of MoO_3 (i.e., 27% expected) calculated from the initial mass.

Thermal decomposition of K_5(**{Mo_3}-ox**)$_2$Cl·9.75 H_2O was found to proceed in three stages (**Figure 12B**)**.** The first loss (Δ = 7% vs calcd. 9%) between 40-100°C corresponds to dehydration of the solid. Subsequent thermal oxidation of $C_2O_4^{2-}$ (Δ = 24% vs calcd. 27%) into CO_2 then takes place between 220-310°C. The small weight loss (Δ = 4% vs calcd. 21%) observed between 310-410°C is ascribed to the loss of the S atoms into SO_2 with the concomitant uptake of oxygen to give MoO_3 and K_2O as ultimate calcinated phases. Overall, the compound exhibits a total weight loss of 35% with the remaining 65% corresponding to the K_2O and MoO_3 left (calcd. 56%). Analysis by SEM-EDS indeed confirmed that the residue was composed mostly by K_2O and MoO_3 based on the following atomic ratios observed compared against the ratio from the formula: 6:4.2 Mo:K (vs 6:5), 6:0.9 Mo:S (vs 6:14), and 6:0 Mo:Cl (vs 6:1). In conclusion, TGA validates the proposed chemical formulas to an extent as the calculated weight % losses approximate the observed losses on the TG curves except for the last decomposition stages (above 300°C).

This is probably because the weight change at this point cannot be fully attributed to the loss of the sulfur atoms as simultaneous uptake of O_2 to form solid metal oxides also occurs.

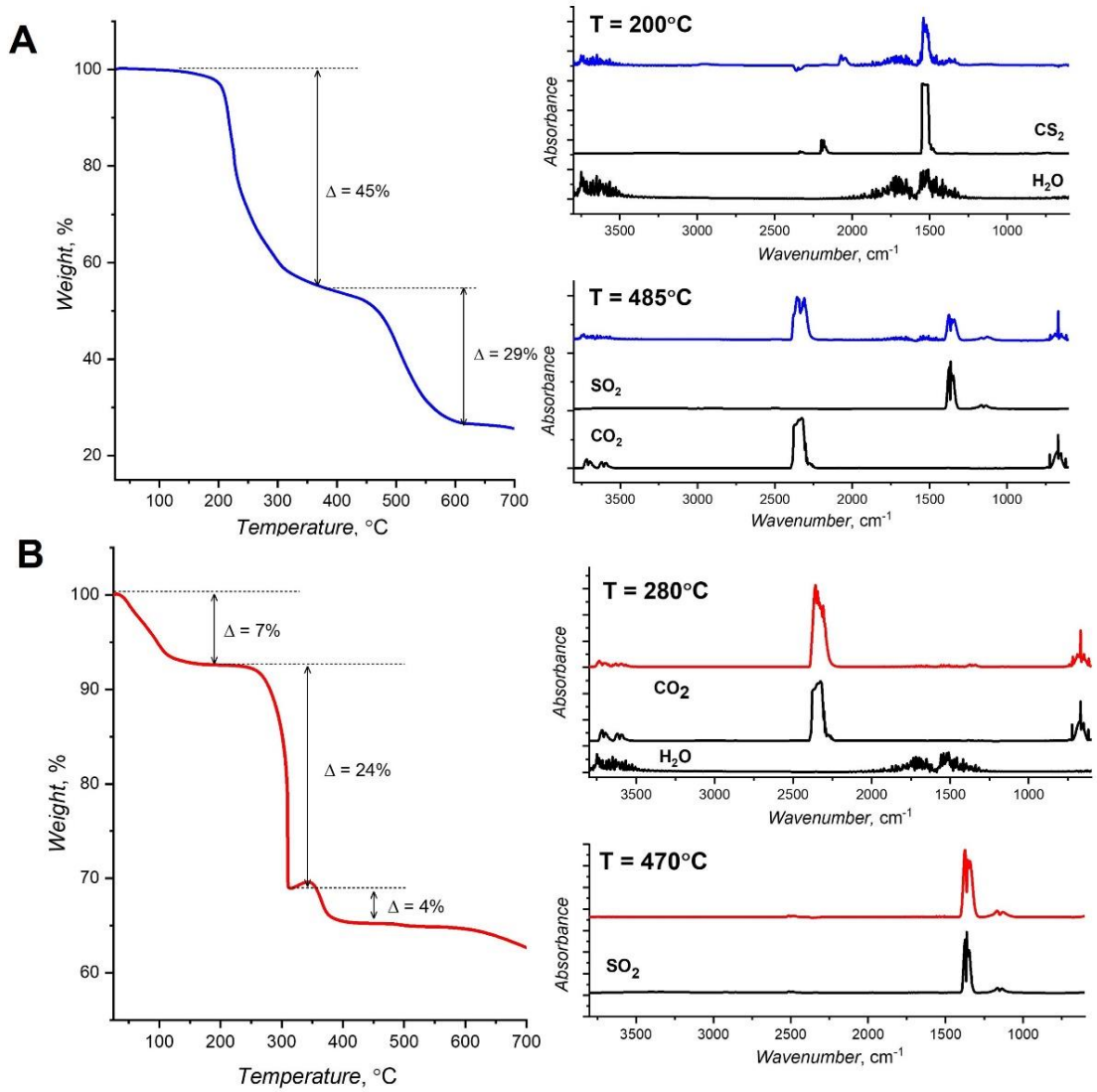

Figure 12. Thermogravimetric curves of (A) $(NBu_4)_2$**{Mo_3}-dmit** and (B) K_5(**{Mo_3}-ox**$)_2Cl)\cdot 9.75\ H_2O$ and the FTIR spectra of the gas released at the given temperatures compared with the spectra of the references (*black*).

2. Electrocatalytic Activity of the {Mo_3S_7} Complexes for HER

2.1 Optimization of the Modified Electrode

To investigate the HER activity of the thiomolybdate complexes, the surface of a glassy carbon (GC) electrode was modified by drop-cast deposition of catalytic inks prepared from the blend of the compound, carbon black (Vulcan XC-72R), and solvent. Several inks were prepared varying the catalyst/carbon ratio, solvent, and presence of the proton conducting Nafion®, to determine the composition that would display the best catalytic performance. Tetrabutylammonium salts of **{Mo_3}-dmit** and **{Mo_3}-ox** were used in the preparation of the catalytic inks considering their low solubility in acidic aqueous media. The results presented are reported in terms of the current density (in mA cm^{-2}) that have been normalized to the electrode geometric area and potentials converted to the reversible hydrogen electrode (RHE) scale (in V_{RHE}). The linear sweep voltammetry (LSV), chronoamperometry, and chronopotentiometry measurements were all carried out in 0.5 M H_2SO_4 employing a conventional three-electrode setup with a rotating disk working electrode maintained at 2500 rpm.

The polarization curves (j-E_{RHE}) in **Figure 13** provide evidence of the HER activity of the thiomolybdate complexes as indicated by the sharp increase in the cathodic current as the applied potential is increased. In contrast, in the absence of the compound, the bare GC electrode remains inert towards H_2 evolution within the relevant potential window.

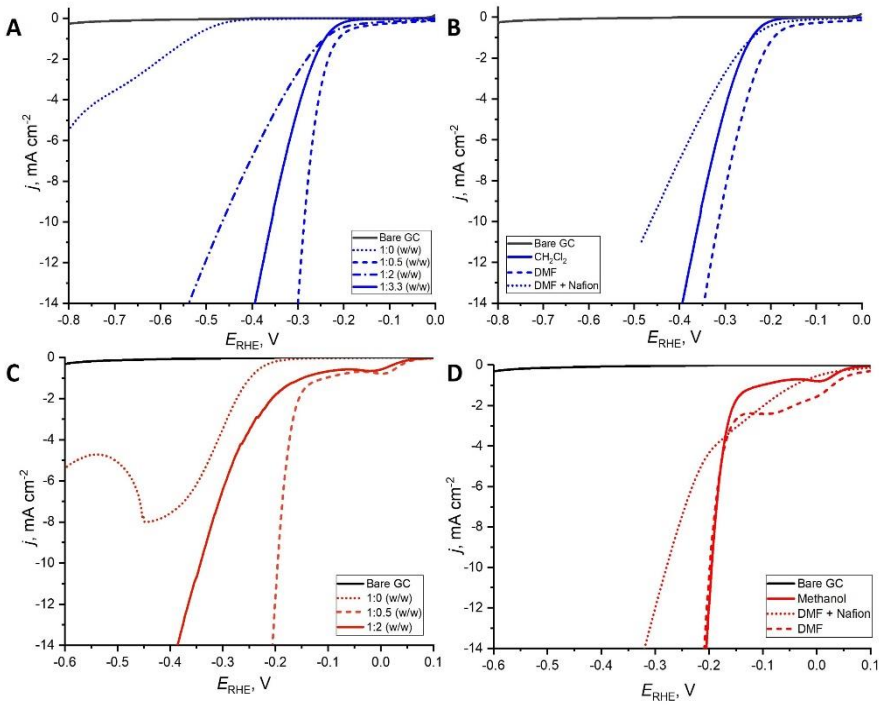

Figure 13. Linear sweep voltammetry measurements (v = 5 mV s^{-1}) of different catalytic inks: (A) variation of the **{Mo$_3$}-dmit**/carbon ratio in CH_2Cl_2 and (B) solvents at fixed 1:3.3 **{Mo$_3$}-dmit**/carbon ratio; (C) variation of the **{Mo$_3$}-ox**/carbon ratio in methanol and (D) solvents at fixed 1:0.50 **{Mo$_3$}-ox**/carbon ratio

The LSV studies also highlight the influence of the solvent and the relative amount of carbon on the performance of the catalyst under the conditions applied. Evidently, the activities are not a direct function of the catalyst/carbon (**Figure 13A and C**) and the best activity for both compounds was observed with 1:0.50 catalyst/carbon ratio. With this composition, we reached low onset potentials (-0.20 V for **{Mo$_3$}-dmit,** -0.14 V for **{Mo$_3$}-ox**) and low η at j = 10 mA cm^{-2} (-0.28 V for **{Mo$_3$}-dmit**, -0.20 V for **{Mo$_3$}-ox**). Carbon is critical for enhancing the conductivity as well as increasing the surface area onto which the catalyst active sites are dispersed. However, large amounts of carbon compromise the mechanical integrity of the material deposited on the electrode leading to detachment issues and loss of activity during measurements. On the other hand, the absence of carbon results in inferior performances with higher overpotentials because of the reduced conductivity.

As illustrated in **Figure 13B** and **D**, the activity is also affected by the solvent which plays an essential role in the uniform deposition of the catalyst. Based on the LSV curves obtained for each solvent condition, the catalytic inks in DMF display the optimal activity for both compounds with onset potentials and η of -0.17 V and -0.31 V, respectively, for **{Mo$_3$}-dmit** and -0.14 V and -0.20 V, respectively, for **{Mo$_3$}-ox**. Nonetheless, CH_2Cl_2 also shows comparable activity for **{Mo$_3$}-dmit** (onset = -0.21 V, η = -0.36 V) and more so with the methanol for the **{Mo$_3$}-ox** (onset = -0.14 V, η = -0.20 V). Even though DMF is excellent, it was not used, however, in the subsequent measurements because CH_2Cl_2 and methanol were demonstrated to have better reproducibility and more homogeneous deposition. The catalytic inks with Nafion® performed the least although its addition greatly minimized the detachment of the catalyst from the electrode surface.

2.2 The HER Activity of $[Mo_3S_7(dmit)_3]^{2-}$

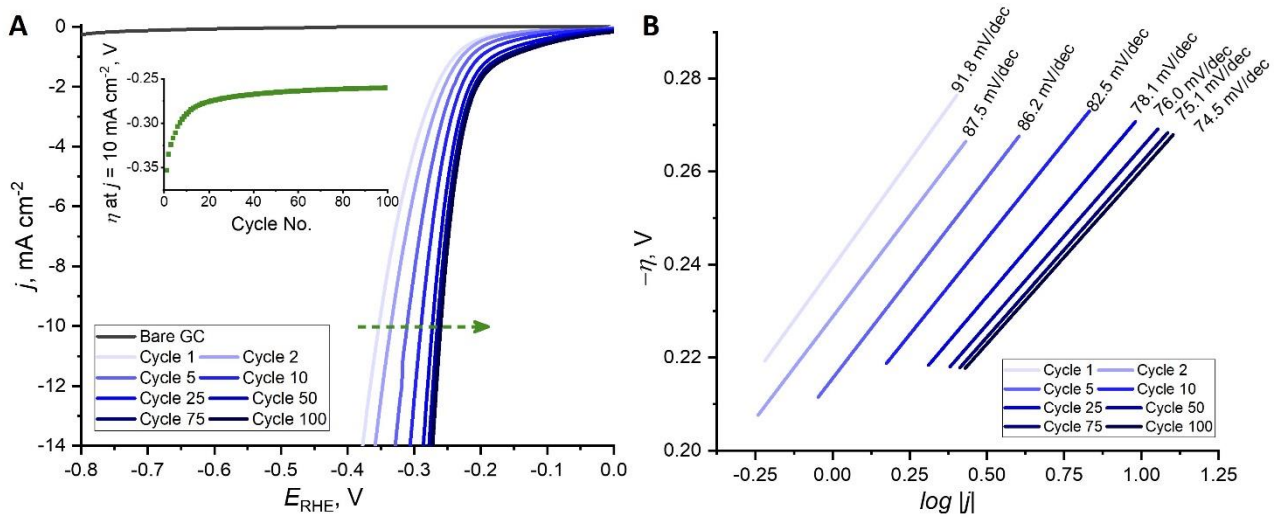

Figure 14. (A) The progress of the polarization curves of $(NBu_4)_2$**{Mo_3}-dmit** during 100 cycles of LSV measurements. The inset shows the evolution of η at j = 10 mA cm^{-2} over the 100 cycles. (B) Tafel plots corresponding to the polarization curves in (A).

Polarization curves of **{Mo_3}-dmit** were obtained for 100 potential cycles to assess the stability of its catalytic activity. As shown in **Figure 14A**, we observe a remarkable shift of the E_{RHE} (at j = 10 mA cm^{-2}) from -0.35 V to less negative values eventually reaching a limiting value of -0.26 V as the cycling progresses. In addition, the corresponding Tafel plots in **Figure 14B** show an apparent decrease of the Tafel slope from 91.8 mV dec^{-1} in the first cycle to 74.5 mV dec^{-1} in the 100th cycle. From these results, we can gather that **{Mo_3}-dmit** exhibits stability and the decreasing overpotential and Tafel slope signifies that the catalyst undergoes an activation behavior. The recorded Tafel slopes for **{Mo_3}-dmit** are slightly higher than the reported Tafel slopes of $[Mo_3S_{13}]^{2-}$ (38-40 mV dec^{-1} and 57 mV dec^{-1} on graphite paper (GP) and HOPG substrate, respectively)[13] and much higher when compared to Pt which has known Tafel slope of ~30 mV per decade[22].

The Tafel slope, aside from being a metric of activity, can also help provide insights into the mechanism of electron transfer kinetics. In the context of HER mechanism, the value of the Tafel slope depends on whether the rate limiting step is the Volmer (120 mV dec^{-1}), Heyrovsky (40 mV dec^{-1}), or Tafel step (30 mV dec^{-1})[22]. Because the observed value of the Tafel slopes (between 74.5 and 91.8 mV dec^{-1}) do not compare with any of the mechanism described, we speculate that the HER activity of **{Mo_3}-dmit** involves a different pathway. Furthermore, the activation towards HER may be a result of an underlying chemical rearrangement involving the complex. To have conclusive evidence for this, analysis of the catalyst on the electrode surface before and after potential cycling must be carried out using spectroscopic techniques such as XPS and Raman.

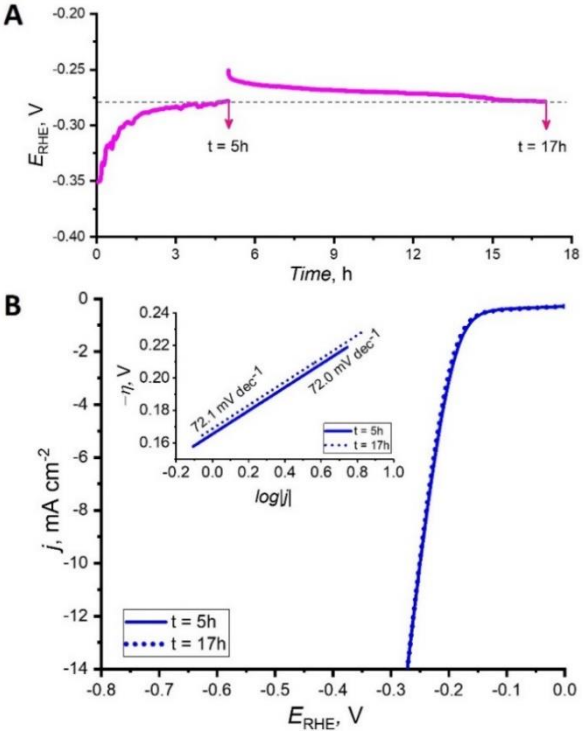

Figure 15. (A) Chronopotentiometry of **{Mo_3}-dmit** at j = 10 mA cm^{-2} for 17 h and the (B) LSV measurements at t = 5h and 17 h and the corresponding Tafel plots in the inset.

In an effort to further examine the extent of the stability of the HER activity of **{Mo_3}-dmit**, chronopotentiometry at a fixed current density of 10 mA cm^{-2} over a period of 17 h was performed. As evidenced in **Figure 15A**, the potential rises in the first 2 h from -0.35 V until it reaches a steady value of -0.28, once again demonstrating the activation of the catalyst. The chronoamperometry was interrupted at t = 5 h to perform LSV before resuming and measuring potential again for the next 12 h. Until the end, the potential value was observed to marginally change only by less than 30 mV. In addition, comparison of the polarization curves obtained after 5 h and 17 h shows that the two completely coincides and the Tafel slope did not change at 72 mV dec^{-1}. Overall, these data demonstrate the impressive durability of the HER activity of **{Mo_3}-dmit** over time under the experimental conditions.

Finally, the efficiency of **{Mo_3}-dmit** as an HER catalyst was evaluated by carrying out bulk electrolysis in 0.5 M H_2SO_4 at a fixed potential E_{RHE} = -0.39 V. The H_2 gas evolved was quantified through an online gas chromatography (GC) equipment (**Figure 16A**). Electrolysis was done only over a period of 6 h but the measurement of H_2 by GC was extended to 3 h more to ensure that all H_2 evolved is accounted. An induction period in the H_2 production was observed in the first 30 mins which may be ascribed to the activation of the catalyst that is reflected in the initial rise in the current density as shown in the chronoamperogram (**Figure 16B**). However, this may also correspond to the time it takes to fill the dead-volume between the working electrode and the GC loop that detects H_2. After, the H_2 generated continues to constantly increase in the next 1.5 hours until the concentration reaches a plateau.

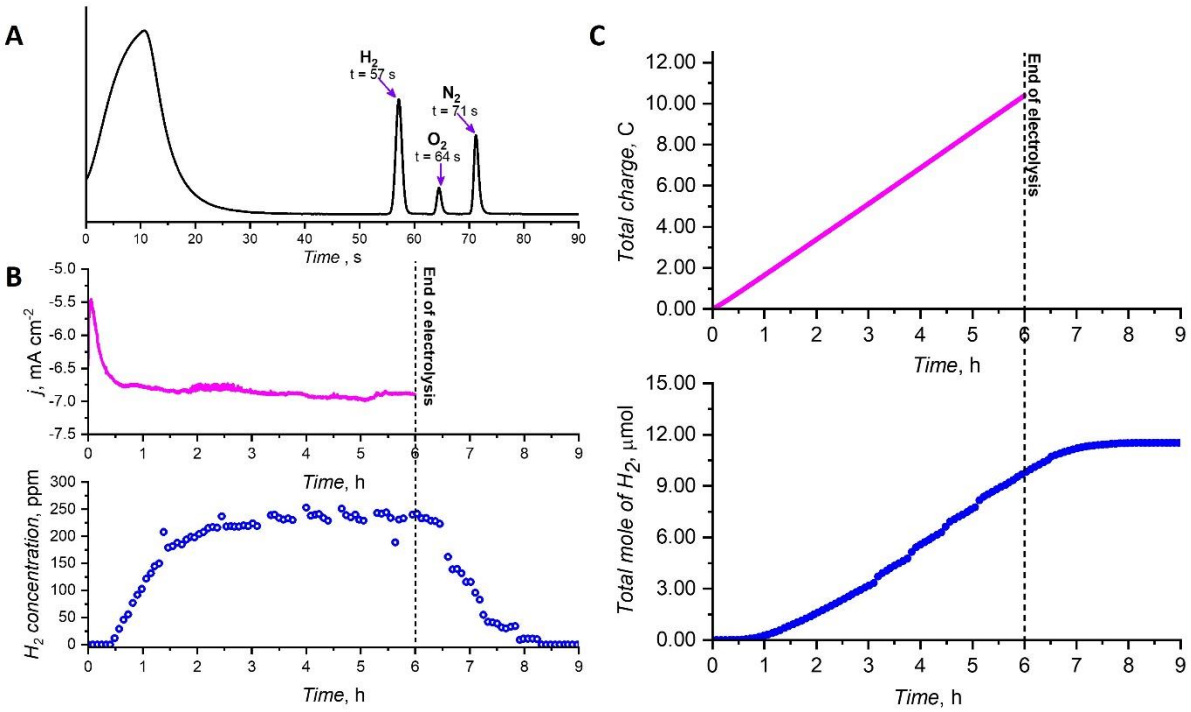

Figure 16. (A) A sample chromatogram obtained by gas chromatography. (B) Chronoamperogram of the bulk electrolysis (*top*) and the concentration (in ppm) of H_2 evolved over time (*bottom*). (C) Total charge input (in C) over time (*top*) and the total moles of H_2 over time (*bottom*) calculated from the H_2 concentration measured and the carrier gas flow rate.

The plot of the total moles of H_2 over time (**Figure 16C**) highlights the stable and constant production of H_2 by the catalyst. Unfortunately, the faradaic efficiency determined from the experiment was only 21%. This very low yield may be due primarily to problems of gas leakage. Similar low yields but inconsistent values were obtained from several trials despite ensuring careful controls on the various potential leak areas. Further optimization of the setup with gas leak tests and possibly recalibration of the GC device must be done to obtain a reliable faradaic efficiency that is expected to be close to 100%.

2.3 The HER Activity of $[Mo_3S_7(ox)_3]^{2-}$

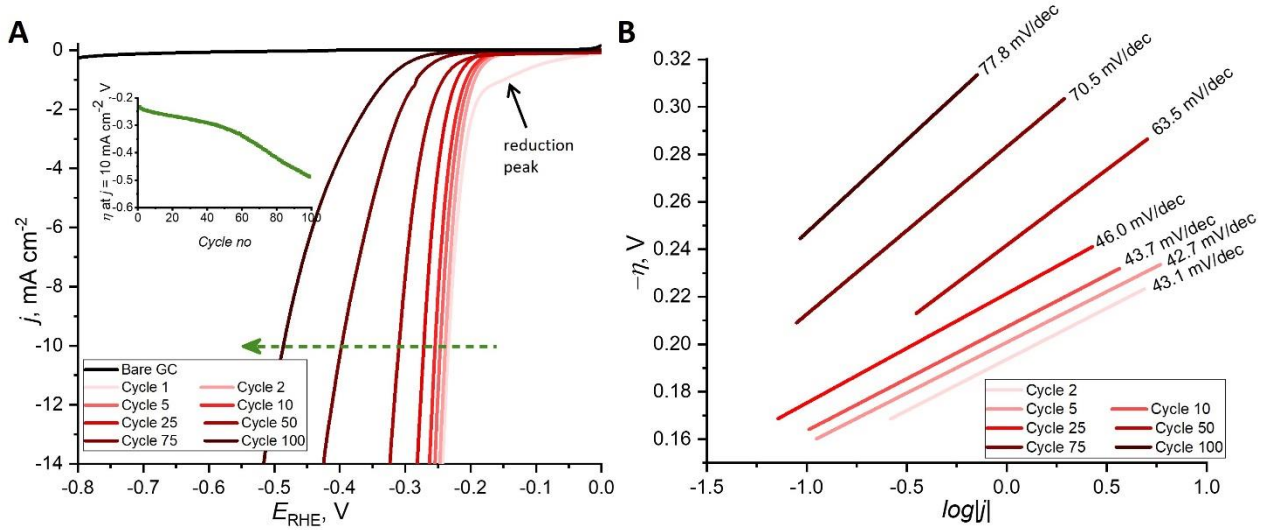

Figure 17. (A) Progress of the polarization curves of $(NBu_4)_2$**{Mo_3}-ox** during 100 cycles of LSV measurements. The inset shows the evolution of η at j = 10 mA cm^{-2} over the 100 cycles. (B) Tafel plots corresponding to the polarization curves in (A)

During the first ten LSV cycles, **{Mo_3}-ox** exhibits better activity compared with the **{Mo_3}-dmit.** The onset potentials and η (at j = 10 mA cm^{-2}) are lower with values ranging between –0.18 to -0.19 V and -0.23 to -0.25 V, respectively (vs the onset potentials between -0.19 to -0.22 V and η between -0.29 to -0.35 V for **{Mo_3}-dmit**). However, throughout 100 potential cycles, the catalyst clearly loses activity as the polarization curve shifts further to more negative potentials (**Figure 17A**). Correspondingly, the Tafel slopes increases from 43.1 mV dec^{-1} to 77.8 mV dec^{-1} which follows the loss of activity on successive potential scanning.

One possible explanation for the instability of **{Mo_3}-ox** is the desorption of the catalyst from the electrode surface. In contrast with **{Mo_3}-dmit**, the **{Mo_3}-ox** complex can desorb more facilely into the aqueous medium because it bears hydrophilic oxalate ligands that can form strong hydrogen bonds with water molecules. Electrochemical deactivation of the catalyst is also a possible reason as evidenced by a small reduction peak that can be seen around -0.15 V_{RHE}. Intriguingly, this reduction event was observed only in the first LSV cycle and was absent in the subsequent potential cycles. We hypothesized that this peak arises from the reduction involving the oxalate ligand that can lead to its dissociation from the $\{Mo_3S_7\}$ core and subsequent exchange with water molecules to form $[Mo_3S_7(ox)_{3-x}(H_2O)_{2x}]^{(2x-2)}$ species that retains the HER activity. In fact, theoretical and experimental investigations by Dave M. et al. (2018) uncovered the effect of ligand-exchange by water on the activity of $[Mo_3S_{13}]^{2-}$ for homogeneous light-driven HER. The results revealed that partial replacement of the terminal disulfides with aquo ligands converts the cluster into the most active species while complete substitution decreased the activity[23]. Based on these findings, we suppose that **{Mo_3}-ox** undergoes a similar process. The HER activity observed originated mainly from the partial formation of the aquo species and the complete exchange of the oxalate ligands with water causes the deactivation of the catalyst and its desorption from the electrode ultimately leading to diminished activity.

2.4 Insights into the Mechanism of $[Mo_3S_7(ox)_3]^{2-}$ Reduction

To understand the nature of the reduction peak in the polarization curve of **{Mo_3}-ox**, we studied the electrochemical behavior of the complex in 0.5 M HSO_4^-/SO_4^{2-} buffer (pH 1.0) by cyclic voltammetry (CV) using an Ag/AgCl (saturated KCl) reference electrode. Evidently, the voltammograms display an irreversible reduction peak around -0.35 $V_{Ag/AgCl}$ with an increasing cathodic peak current, i_{pc}, as a linear function of the concentration of **{Mo_3}-ox** (**Figure 18A**). The sudden rise of current at more negative

potentials is associated to proton reduction, suggesting that the complex also facilitate HER in homogeneous phase. To determine whether the redox behavior is centered on the oxalate ligand as speculated, we examined the effect of the addition of oxalic acid (denoted H_2ox). Indeed, the i_{pc} increases with the amount of H_2ox until a saturation point is reached where the current no longer changes with any additional H_2ox (**Figure 18B**). Furthermore, as shown in **Figure 18C,** we found that oxalate ion alone does not show electrochemical behavior in the considered potential range suggesting the role of $\{Mo_3S_7\}$ in mediating the observed reduction process.

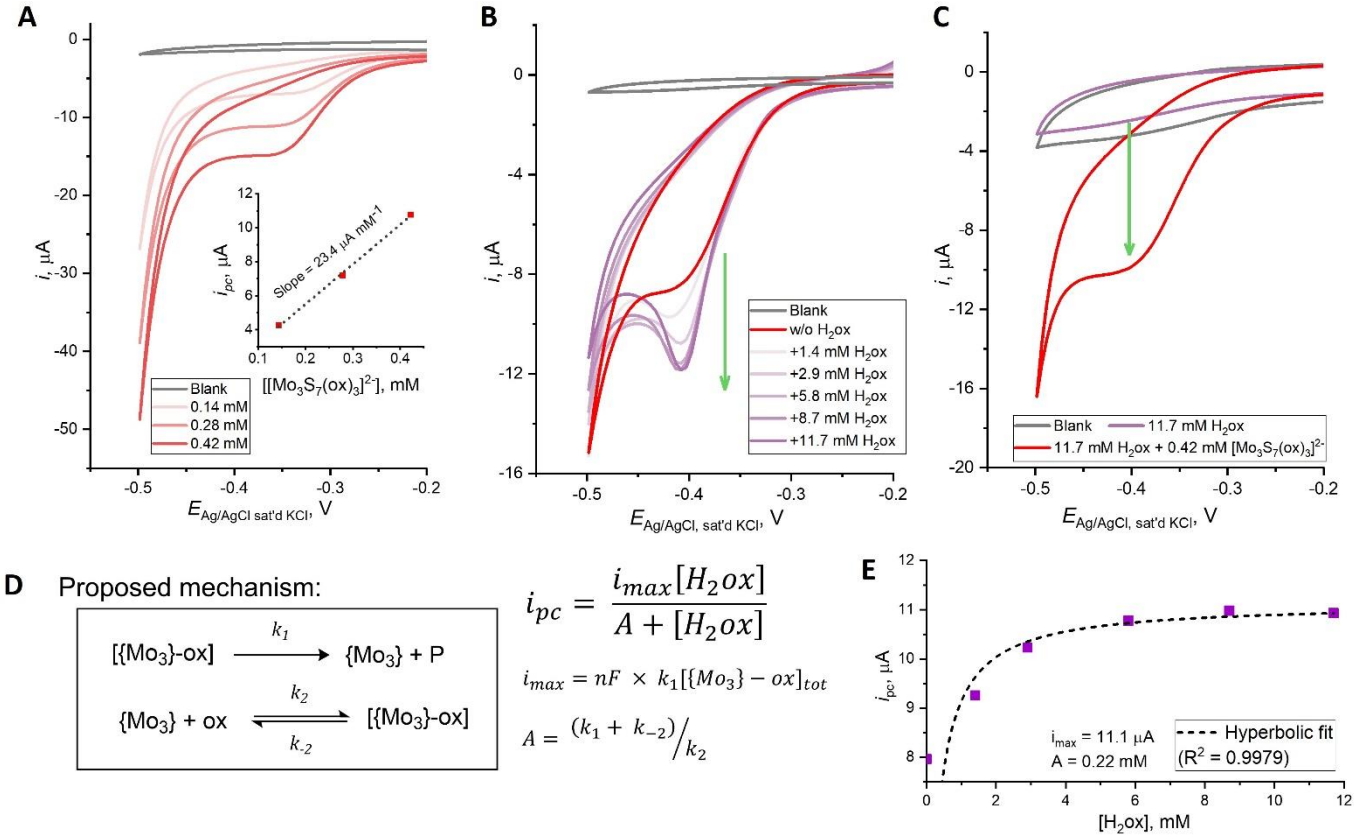

$$i_{pc} = \frac{i_{max}[H_2ox]}{A + [H_2ox]}$$

$$i_{max} = nF \times k_1[\{Mo_3\} - ox]_{tot}$$

$$A = {(k_1 + k_{-2})}/{k_2}$$

Figure 18. Cyclic voltammetry studies of **{Mo$_3$}-ox** in 0.5 M HSO_4^-/SO_4^{2-} buffer (pH 1.0): dependence of the cathodic peak current, i_{pc}, on the concentration of **{Mo$_3$}-ox** (A) and [H_2ox] (at a fixed [**{Mo$_3$}-ox**] = 0.42 mM) (B), the effect of adding **{Mo$_3$}-ox** to H_2ox (C), the proposed mechanism (D) and the nonlinear regression of the observed i_{pc} vs [H_2ox] based on the equation derived from the model proposed (E). The ionic charges of the species are not shown to avoid confusion. n – number of electrons, F – Faraday's constant (96485 C mol^{-1}), k_1, k_2, *and* k_{-2} – rate constants, and A – constant equal to $(k_1 + k_{-2})/k_2$

From these results, we propose a mechanism resembling the form of the Michaelis-Menten model (**Figure 18D**). In the model, the first step involves a slow, irreversible first-order reaction that converts the oxalate ligand into product P leaving a naked **{Mo$_3$}** that can freely coordinate with water or other anions. This is followed by a fast, reversible second-order step where **{Mo$_3$}-ox** is regenerated by the binding of another oxalate anion. Through these assumptions, we were able to derive a mathematical equation that describes the observed hyperbolic relation between i_{pc} and H_2ox concentration (**Figure 18E**). The equation introduces two parameters: the maximum cathodic current i_{max} and the constant A. The maximum current is a function of the total concentration of **{Mo$_3$}-ox**. At a fixed **{Mo$_3$}-ox** concentration, the current initially increases the addition of H_2ox replenishes **{Mo$_3$}-ox**. At higher H_2ox concentrations, however, the i_{max} is reached due to the limiting rate of electrochemical conversion of the complex to form the naked **{Mo$_3$}**.

The voltammetric study of **{Mo$_3$}-ox** was also done in different pH of 0.5 M HSO_4^-/SO_4^{2-} buffer (pH 1.0, 1.3, and 1.7) to see the effect of proton concentration on the reduction. From the plot of the

cathodic peak potential, E_{pc}, against pH (**Figure 19**), we obtained a slope equal to almost twice -59 mV/pH (i.e., -123 mV/pH) implying a reduction process that involves $2n$ H^+/ n e^- (n = 1, 2, 3, …). Based on literature, we hypothesize that oxalic acid gets reduced to glyoxylic acid[24], although further investigations (by NMR or HPLC-MS) must still be carried out to confirm the identity of the product. Nevertheless, this opens an opportunity to explore the relevance of thiomolybdate clusters in the electrocatalytic conversion of oxalic acid into value-added chemicals that can be viewed as part of the valorisation of the products resulting from CO_2 reduction.

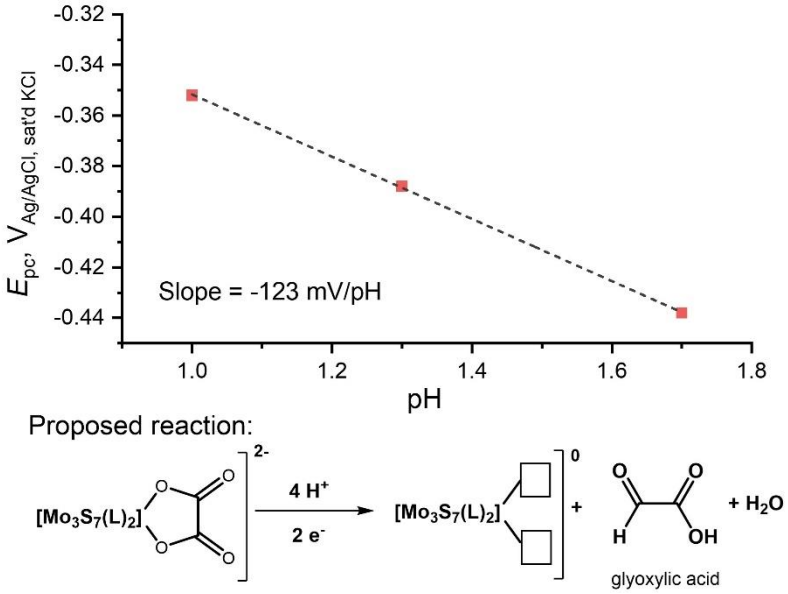

Figure 19. Plot of E_c in terms of $V_{Ag/AgCl}$ as a function of pH (*top*) and the proposed chemical equation of the reduction of oxalate to glyoxylic acid *(bottom)* (L = *ox*)

Conclusion and Perspectives

Here, we have presented the synthesis and physical characterization of two molecular thiomolybdate complexes based on the $\{Mo_3S_7\}$ cluster and illustrated their electrocatalytic activity towards hydrogen evolution. The transmetalation of $[Mo_3S_7Cl_6]^{2-}$ with the proligand $Bu_2Sn(dmit)$ produced $[Mo_3S_7(dmit)_3]^{2-}$ with a fair yield while ligand substitution of the same precursor with oxalic acid resulted in $[Mo_3S_7(ox)_3]^{2-}$ with an excellent yield. The crystal structures of both compounds determined by XRD revealed interesting supramolecular arrangements arising from the non-covalent S···S and S···Cl interactions involving the electrophilic axial S atoms of the cluster in $[Mo_3S_7(dmit)_3]^{2}$ and $[Mo_3S_7(ox)_3]^{2}$, respectively. Powder XRD confirmed the homogeneity and purity of the products. Meanwhile, TGA combined with FTIR, and EDS analysis enabled the rough estimation of the ratios of the components of the two compounds. While the experimentally observed weight losses in the initial stages of the TG curves approximately matches the expected weight losses calculated from the chemical formulas, the latter weight losses (T > 300°C) cannot be unambiguously interpreted due to the possible simultaneous uptake of O_2 to form metal oxides.

We found from electrochemical studies of the complexes drop-cast on a glassy carbon electrode that both $[Mo_3S_7(dmit)_3]^{2-}$ and $[Mo_3S_7(ox)_3]^{2-}$ exhibit high HER activities in acidic medium. The optimal composition of the catalytic inks was empirically determined by varying the catalyst/carbon ratio, solvent, and the presence of Nafion. To achieve a 10-mA cm^{-2} current density, $[Mo_3S_7(dmit)_3]^{2-}$ requires an η of -0.35 V_{RHE} that decreases as the catalyst gets activated with potential cycling. This is also accompanied by a decreasing Tafel slope that led us to speculate that the catalyst is activated by undergoing some chemical rearrangement. Chronopotentiometry for 17 h and LSV for 100 cycles further demonstrated the excellent stability of the activity of $[Mo_3S_7(dmit)_3]^{2-}$. In contrast, $[Mo_3S_7(ox)_3]^{2-}$ initially displayed a higher HER activity with an initial η of -0.23. However, the unstable activity of $[Mo_3S_7(ox)_3]^{2-}$ declined with successive potential scanning. Such a deactivation process could result from the electrochemical reduction of the coordinated oxalate ligands and their subsequent replacements by water. A desorption of the active material can also occur resulting from the release of the hydrophilic oxalate complex from the electrode surface to the bulk electrolytic aqueous solution. Cyclic voltammetry indeed provided evidence of the reduction of the oxalate ligands in the $[Mo_3S_7(ox)_3]^{2-}$ catalyst and hints at the possible role of $\{Mo_3S_7\}$ core in facilitating this reaction.

Taken together, these findings show the potential of molecular thiomolybdate species as electrocatalysts for HER. We have shown that the nature of the ligand modulates both the HER activity and stability of the catalyst and suggests that the properties of thiomolybdate cluster complexes can be fine-tuned and optimized by ligand design. The use of non-innocent dithiolene ligands proves to be promising as they can impart specific structural and electronic effects that may contribute to the stability and increased activity. Furthermore, with further optimization of $[Mo_3S_7(dmit)_3]^{2-}$ and $[Mo_3S_7(ox)_3]^{2-}$, we envisage the possibility of their incorporation as catalytic components of the cathode electrode of proton exchange membranes (PEM) under industrial conditions.

References

[1] Staffell, I.; Scamman, D.; Velazquez Abad, A.; Balcombe, P.; Dodds, P. E.; Ekins, P.; Shah, N.; Ward, K. R. The Role of Hydrogen and Fuel Cells in the Global Energy System. *Energy Environ. Sci.* **2019**, *12* (2), 463–491. https://doi.org/10.1039/C8EE01157E.

[2] IEA report. https://iea.blob.core.windows.net/assets/5bd46d7b-906a-4429-abda-e9c507a62341/GlobalHydrogenReview2021.pdf

[3] Newborough, M.; Cooley, G. Developments in the Global Hydrogen Market: The Spectrum of Hydrogen Colours. *Fuel Cells Bulletin* **2020**, *2020* (11), 16–22. https://doi.org/10.1016/S1464-2859(20)30546-0.

[4] Wang, S.; Lu, A.; Zhong, C.-J. Hydrogen Production from Water Electrolysis: Role of Catalysts. *Nano Convergence* **2021**, *8* (1), 4. https://doi.org/10.1186/s40580-021-00254-x.

[5] Grutza, M.-L.; Rajagopal, A.; Streb, C.; Kurz, P. Hydrogen Evolution Catalysis by Molybdenum Sulfides (MoS_x): Are Thiomolybdate Clusters like $[Mo_3S_{13}]^{2-}$ Suitable Active Site Models? *Sustainable Energy Fuels* **2018**, *2* (9), 1893–1904. https://doi.org/10.1039/C8SE00155C.

[6] Laursen, A. B.; Kegnæs, S.; Dahl, S.; Chorkendorff, I. Molybdenum Sulfides—Efficient and Viable Materials for Electro - and Photoelectrocatalytic Hydrogen Evolution. *Energy Environ. Sci.* **2012**, *5* (2), 5577. https://doi.org/10.1039/c2ee02618j.

[7] Jaramillo, T. F.; Jørgensen, K. P.; Bonde, J.; Nielsen, J. H.; Horch, S.; Chorkendorff, I. Identification of Active Edge Sites for Electrochemical H_2 Evolution from MoS_2 Nanocatalysts. *Science* **2007**, *317* (5834), 100–102. https://doi.org/10.1126/science.1141483.

[8] Benck, J. D.; Hellstern, T. R.; Kibsgaard, J.; Chakthranont, P.; Jaramillo, T. F. Catalyzing the Hydrogen Evolution Reaction (HER) with Molybdenum Sulfide Nanomaterials. ACS Catal. 2014, 4 (11), 3957–3971. https://doi.org/10.1021/cs500923c.

[9] Zaman, N.; Noor, T.; Iqbal, N. Recent Advances in the Metal–Organic Framework-Based Electrocatalysts for the Hydrogen Evolution Reaction in Water Splitting: A Review. RSC Adv. 2021, 11 (36), 21904–21925. https://doi.org/10.1039/D1RA02240G.

[10] Samantara, A. K.; Ratha, S. Mechanism and Key Parameters for Catalyst Evaluation. In Metal Oxides/Chalcogenides and Composites; SpringerBriefs in Materials; Springer International Publishing: Cham, 2019; pp 11–29. https://doi.org/10.1007/978-3-030-24861-1_3.

[11] Coucouvanis, D. Syntheses, Structures, and Reactions of Binary and Tertiary Thiomolybdate Complexes Containing the (O)Mo(Sx) AND (S)Mo(Sx) Functional Groups (x = 1, 2, 4). In Advances in Inorganic Chemistry; Elsevier, 1998; Vol. 45, pp 1–73. https://doi.org/10.1016/S0898-8838(08)60024-0.

[12] Jaramillo, T. F.; Bonde, J.; Zhang, J.; Ooi, B.-L.; Andersson, K.; Ulstrup, J.; Chorkendorff, I. Hydrogen Evolution on Supported Incomplete Cubane-Type $[Mo_3S_4]^{4+}$ Electrocatalysts. J. Phys. Chem. C 2008, 112 (45), 17492–17498. https://doi.org/10.1021/jp802695e.

[13] Kibsgaard, J.; Jaramillo, T. F.; Besenbacher, F. Building an Appropriate Active-Site Motif into a Hydrogen-Evolution Catalyst with Thiomolybdate [Mo3S13]2– Clusters. Nature Chem 2014, 6 (3), 248–253. https://doi.org/10.1038/nchem.1853.

[14] Lee, C.-H.; Lee, S.; Lee, Y.-K.; Jung, Y. C.; Ko, Y.-I.; Lee, D. C.; Joh, H.-I. Understanding the Origin of Formation and Active Sites for Thiomolybdate [Mo 3 S 13] 2– Clusters as Hydrogen Evolution Catalyst through the Selective Control of Sulfur Atoms. ACS Catal. 2018, 8 (6), 5221–5227. https://doi.org/10.1021/acscatal.8b01034.

[15] Qiu, T.; Liang, Z.; Guo, W.; Tabassum, H.; Gao, S.; Zou, R. Metal–Organic Framework-Based Materials for Energy Conversion and Storage. ACS Energy Lett. 2020, 5 (2), 520–532. https://doi.org/10.1021/acsenergylett.9b02625.

[16] Stassen, I.; Burtch, N.; Talin, A.; Falcaro, P.; Allendorf, M.; Ameloot, R. An Updated Roadmap for the Integration of Metal–Organic Frameworks with Electronic Devices and Chemical Sensors. Chem. Soc. Rev. 2017, 46 (11), 3185–3241. https://doi.org/10.1039/C7CS00122C.

[17] Sun, L.; Campbell, M. G.; Dincă, M. Electrically Conductive Porous Metal-Organic Frameworks. Angew. Chem. Int. Ed. 2016, 55 (11), 3566–3579. https://doi.org/10.1002/anie.201506219.

[18] Ji, Z.; Trickett, C.; Pei, X.; Yaghi, O. M. Linking Molybdenum–Sulfur Clusters for Electrocatalytic Hydrogen Evolution. J. Am. Chem. Soc. 2018, 140 (42), 13618–13622. https://doi.org/10.1021/jacs.8b09807.

[19] Cadot, E.; Sokolov, M. N.; Fedin, V. P.; Simonnet-Jégat, C.; Floquet, S.; Sécheresse, F. A Building Block Strategy to Access Sulfur-Functionalized Polyoxometalate Based Systems Using {Mo2S2O2} and {Mo3S4} as Constitutional Units, Linkers or Templates. Chem. Soc. Rev. 2012, 41 (22), 7335. https://doi.org/10.1039/c2cs35145e.

[20] Llusar, R.; Uriel, S.; Vicent, C.; Clemente-Juan, J. M.; Coronado, E.; Gómez-García, C. J.; Braïda, B.; Canadell, E. Single-Component Magnetic Conductors Based on Mo 3 S 7 Trinuclear Clusters with Outer Dithiolate Ligands. J. Am. Chem. Soc. 2004, 126 (38), 12076–12083. https://doi.org/10.1021/ja0474244.

[21] Sokolov, M. N.; Gushchin, A. L.; Naumov, D. Yu.; Gerasko, O. A.; Fedin, V. P. Cluster Oxalate Complexes [M 3 (μ 3 -Q)(μ 2 -Q 2) 3 (C 2 O 4) 3] 2 - and [Mo 3 (μ 3 -Q)(μ 2 -Q) 3 (C 2 O 4) 3 (H 2 O) 3] 2 - (M = Mo, W; Q = S, Se): Mechanochemical Synthesis and Crystal Structure. Inorg. Chem. 2005, 44 (7), 2431–2436. https://doi.org/10.1021/ic0488637.

[22] McAllister, J.; Bandeira, N. A. G.; McGlynn, J. C.; Ganin, A. Y.; Song, Y.-F.; Bo, C.; Miras, H. N. Tuning and Mechanistic Insights of Metal Chalcogenide Molecular Catalysts for the Hydrogen-Evolution Reaction. Nat Commun 2019, 10 (1), 370. https://doi.org/10.1038/s41467-018-08208-4.

[23] Dave, M.; Rajagopal, A.; Damm-Ruttensperger, M.; Schwarz, B.; Nägele, F.; Daccache, L.; Fantauzzi, D.; Jacob, T.; Streb, C. Understanding Homogeneous Hydrogen Evolution Reactivity and Deactivation Pathways of Molecular Molybdenum Sulfide Catalysts. Sustainable Energy Fuels 2018, 2 (5), 1020–1026. https://doi.org/10.1039/C7SE00599G.

[24] Abramo, F. P.; De Luca, F.; Passalacqua, R.; Centi, G.; Giorgianni, G.; Perathoner, S.; Abate, S. Electrocatalytic Production of Glycolic Acid via Oxalic Acid Reduction on Titania Debris Supported on a TiO2 Nanotube Array. Journal of Energy Chemistry 2022, 68, 669–678. https://doi.org/10.1016/j.jechem.2021.12.034

[25] Hinnemann, B.; Moses, P. G.; Bonde, J.; Jørgensen, K. P.; Nielsen, J. H.; Horch, S.; Chorkendorff, I.; Nørskov, J. K. Biomimetic Hydrogen Evolution: MoS 2 Nanoparticles as Catalyst for Hydrogen Evolution. J. Am. Chem. Soc. 2005, 127 (15), 5308–5309. https://doi.org/10.1021/ja0504690